

# CO<sub>2</sub>-Assisted Oxidative Dehydrogenation of Propane over VO<sub>x</sub>/In<sub>2</sub>O<sub>3</sub> Catalysts: Interplay between Redox Property and Acid–Base Interactions

Xiao Jiang, Bar Mosevitzky Lis, Stephen C. Purdy, Sreya Paladugu, Victor Fung, Wenying Quan, Zhenghong Bao, Weiwei Yang, Yang He, Bobby G. Sumpter, Katharine Page, Israel E. Wachs,\* and Zili Wu\*



Cite This: *ACS Catal.* 2022, 12, 11239–11252



Read Online

ACCESS |

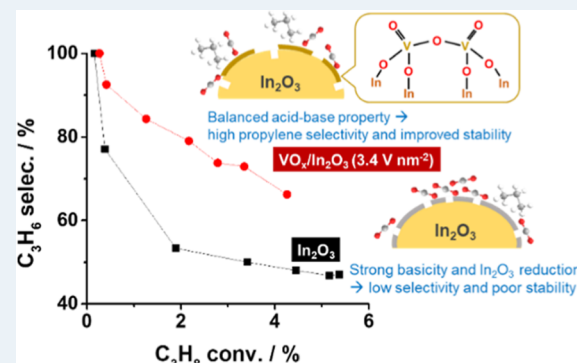
Metrics & More

Article Recommendations

Supporting Information

**ABSTRACT:** In this work, a series of VO<sub>x</sub>-loaded In<sub>2</sub>O<sub>3</sub> catalysts were prepared, and their catalytic performance was evaluated for CO<sub>2</sub>-assisted oxidative dehydrogenation of propane (CO<sub>2</sub>-ODHP) and compared with In<sub>2</sub>O<sub>3</sub> alone. The optimal composition is obtained on 3.4V/In<sub>2</sub>O<sub>3</sub> (surface V density of 3.4V nm<sup>-2</sup>), which exhibited not only a higher C<sub>3</sub>H<sub>6</sub> selectivity than other V/In catalysts and In<sub>2</sub>O<sub>3</sub> under isoconversion conditions but also an improved reaction stability. To elucidate the catalyst structure–activity relationship, the VO<sub>x</sub>/In<sub>2</sub>O<sub>3</sub> catalysts were characterized by chemisorption [NH<sub>3</sub>-temperature-programmed desorption (TPD), NH<sub>3</sub>-diffuse reflectance infrared Fourier transform spectroscopy (DRIFTS), CO<sub>2</sub>-TPD, and CO<sub>2</sub>-DRIFTS], H<sub>2</sub>-temperature-programmed reduction (TPR), in situ Raman spectroscopy, UV-vis diffuse reflectance spectroscopy, near-ambient pressure X-ray photoelectron spectroscopy, X-ray absorption spectroscopy, and further examined using density functional theory. The In–O–V structure and the extent of oligomerization, which play a crucial role in improving selectivity and stability, were identified in the VO<sub>x</sub>/In<sub>2</sub>O<sub>3</sub> catalysts. In particular, the presence of surface VO<sub>x</sub> (i) inhibits the deep reduction of In<sub>2</sub>O<sub>3</sub>, thereby preserving the activity, (ii) neutralizes the excess basicity on In<sub>2</sub>O<sub>3</sub>, thus suppressing propane dry reforming and achieving a higher propylene selectivity, and (iii) introduces additional redox sites that participate in the dehydrogenation reaction by utilizing CO<sub>2</sub> as a soft oxidant. The present work provides insights into developing selective, stable, and robust metal-oxide catalysts for CO<sub>2</sub>-ODHP by controlling the conversion of reagents via desired pathways through the interplay between acid–base interactions and redox properties.

**KEYWORDS:** oxidative dehydrogenation, propane, carbon dioxide, indium oxide, vanadium oxide, acid–base interaction, redox property



## 1. INTRODUCTION

Light alkenes such as propylene (C<sub>3</sub>H<sub>6</sub>) are important building blocks for a large number of chemicals in the petrochemical industry.<sup>1</sup> Conventionally, C<sub>3</sub>H<sub>6</sub> is produced as a byproduct in producing ethylene by steam cracking and fluid catalytic cracking of naphtha, light diesel, and other oil byproducts.<sup>2</sup> Nowadays, there is a discrepancy between the market demand and productivity.<sup>3</sup> To make-up the shortfall of C<sub>3</sub>H<sub>6</sub> supply, the on-purpose C<sub>3</sub>H<sub>6</sub> production technologies such as dehydrogenation of propane (DHP) have been implemented.<sup>2,4,5</sup> However, DHP suffers from intrinsic drawbacks such as thermodynamic restraints which require high reaction temperatures that inevitably result in severe coking and undesired thermal cracking.<sup>6</sup> Moreover, the indispensable addition of extra hydrogen in the feed gas and its regeneration make the process both energy and capital intensive.<sup>7–10</sup>

Due to its exothermicity and limited thermodynamic restraint, oxidative dehydrogenation of propane (ODHP)

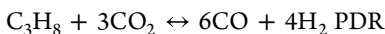
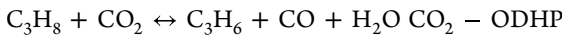
provides alternatives to complement the DHP route.<sup>11</sup> Presently, oxygen (O<sub>2</sub>) has been majorly used as the oxidant for ODHP, and higher C<sub>3</sub>H<sub>6</sub> and light alkene (C<sub>2</sub>–C<sub>3</sub>=) selectivities can be achieved. Representative catalysts include hexagonal boron nitride and boron oxide catalysts through the Eley-Rideal (ER) mechanism<sup>12–18</sup> and redox-active vanadium oxide-based catalysts via a Mars-van Krevelen mechanism (MvK).<sup>1</sup> Over-oxidation to undesired carbon oxides (CO<sub>x</sub>) is the major challenge with O<sub>2</sub> as the oxidant, which reduces the selectivity toward alkenes.<sup>1,19</sup> Furthermore, concerns of process flammability due to the presence of O<sub>2</sub> also

Received: April 28, 2022

Revised: August 23, 2022

exist.<sup>11,20</sup> To tackle these issues, introducing a soft oxidant such as carbon dioxide ( $\text{CO}_2$ ) provides a potential avenue and has been applied in the coupling of methane,<sup>21</sup> dehydrogenation of ethylbenzene,<sup>22</sup> propane,<sup>11,23</sup> and iso-butane.<sup>24</sup> The positive roles of  $\text{CO}_2$  in the overall ODHP reaction include serving as (i) a diluent to enhance the equilibrium conversion of light alkanes and (ii) an agent to remove coke via the reverse Boudouard reaction.<sup>25</sup> Moreover,  $\text{CO}_2$  can help keep the metal components at a higher oxidation state during  $\text{CO}_2$ -ODHP, such as inhibiting the formation of metallic iron and iron carbide with better activity toward isobutane dehydrogenation.<sup>26</sup> Combining  $\text{CO}_2$  with the ODHP reaction can also potentially allow for the utilization of the carbon source from  $\text{CO}_2$  via a hydrogen-free manner.<sup>11</sup>

In addition to ODHP, side reactions include reverse water gas shift (RWGS) and propane dry reforming (PDR) (see reactions below).<sup>11,23,27</sup> There are two proposed reaction cycles. The first scenario proposes that  $\text{CO}_2$ -ODHP is a net reaction of DHP and RWGS, wherein RWGS can help remove the formed  $\text{H}_2$  to form CO and  $\text{H}_2\text{O}$ , therefore boosting the DHP reaction by shifting the reaction equilibrium to the side of forming propylene.<sup>11,28</sup> Alternatively, the reaction can proceed through a one-cycle reaction, in which  $\text{CO}_2$  closes the cycle to produce CO without undergoing a separate RWGS route after the surface undergoes direct propane dehydrogenation.<sup>29</sup> PDR is endothermic, which could result in the increase in CO while a decrease in  $\text{C}_3\text{H}_6$  selectivity at high temperatures. Therefore, designing catalysts that can selectively break the C–H bond to produce alkenes while suppressing PDR is of great interest. Similar to the  $\text{O}_2$ -ODHP route, redox-active metal oxides (Cr and V) are promising candidates for  $\text{CO}_2$ -ODHP.<sup>1,11,30</sup> However, due to the toxic and carcinogenic properties of Cr(VI) oxides, it is vital to find alternatives.<sup>30</sup> Group IIIA mixed oxides such as  $\text{Ga}_2\text{O}_3$ – $\text{Al}_2\text{O}_3$ <sup>31,32</sup> and  $\text{In}_2\text{O}_3$ – $\text{Al}_2\text{O}_3$ <sup>33</sup> and supported  $\text{In}_2\text{O}_3$  catalyst<sup>25,34</sup> show comparable catalytic performance as well. On  $\text{Ga}_2\text{O}_3$ , ODHP is proposed to proceed via the heterolytic propane dissociation on acid–base pairs, namely,  $\text{Ga}^{\delta+}$ – $\text{O}^{2-}$  pairs.<sup>28</sup> Specifically,  $\text{C}_3\text{H}_7^+$  is adsorbed on  $\text{O}^{2-}$  (basic sites), while  $\text{H}^-$  is adsorbed on  $\text{Ga}^{\delta+}$  (acid sites).<sup>28</sup> The presence of  $\text{CO}_2$  aids in facilitating the removal of dissociatively adsorbed  $\text{H}_2$  on acid–base pairs of Ga–O and recovering the active sites for the subsequent C–H activation for propylene formation.<sup>28</sup>



Our interest lies in the  $\text{In}_2\text{O}_3$ -based catalysts because of their comparable  $\text{C}_3\text{H}_6$  selectivity to  $\text{Ga}_2\text{O}_3$  under isoconversional conditions<sup>11</sup> and well-known capability in activating  $\text{CO}_2$  molecules, such as  $\text{CO}_2$  hydrogenation.<sup>35–38</sup> However, the mechanism on  $\text{In}_2\text{O}_3$  for ODHP is still elusive.  $\text{CO}_2$  is a more acidic gas than propane, which might negatively impact the C–H activation of  $\text{C}_3\text{H}_8$  during ODHP.<sup>28</sup> Thus, due to the strong basicity of  $\text{In}_2\text{O}_3$ ,<sup>35–38</sup> it might selectively activate  $\text{CO}_2$  instead of  $\text{C}_3\text{H}_8$  during ODHP. Thus, the unbalanced acid–base properties of  $\text{In}_2\text{O}_3$  is a major challenge for ODHP.<sup>11</sup> In the present work, we propose to incorporate an acidic metal oxide  $\text{VO}_x$  onto the basic  $\text{In}_2\text{O}_3$  to (i) neutralize the excess basic sites (oxygen vacancies and lattice oxygen) with controlled capability of  $\text{CO}_2$  activation and to (ii) improve the reaction

stability through the intimate interaction between  $\text{In}_2\text{O}_3$  and redox-active  $\text{VO}_x$ . Thus, we aim at clarifying the interplay between redox property and acid–base interactions and their relationship with the activity performance and stability in  $\text{CO}_2$ -ODHP. For these purposes, we prepared a series of  $\text{VO}_x$ -loaded  $\text{In}_2\text{O}_3$  catalysts with various surface V densities and evaluated their catalytic performance in  $\text{CO}_2$ -ODHP. To reveal the catalyst composition–structure–activity relationship, a wide array of characterization techniques has been applied, including chemisorption, diffuse reflectance infrared Fourier transform spectroscopy (DRIFTS), near-ambient pressure X-ray photoelectron spectroscopy (NAP-XPS), X-ray absorption spectroscopy (XAS), UV–vis diffuse reflectance spectroscopy (UV–vis DRS), and Raman spectroscopy. Density functional theory (DFT) was also used to study the effect of surface  $\text{VO}_x$  on the formation of oxygen vacancies of  $\text{In}_2\text{O}_3$ .

## 2. EXPERIMENTAL SECTION

**2.1. Catalyst Preparation.**  $\text{In}_2\text{O}_3$  (surface area,  $\sim 70 \text{ m}^2 \text{ g}^{-1}$ ) was prepared by the calcination of  $\text{In}(\text{OH})_3$ , as reported elsewhere.<sup>35</sup> A brief description is provided in the Supporting Information. The crystalline  $\text{V}_2\text{O}_5$  was prepared by calcining the precursor  $\text{NH}_4\text{VO}_3$  at  $550^\circ\text{C}$ . The structure of  $\text{V}_2\text{O}_5$  was characterized by Raman spectroscopy, and the resultant spectrum is shown in Figure S1.

V-loaded  $\text{In}_2\text{O}_3$  catalysts were prepared by impregnation in an aqueous solution of  $\text{NH}_4\text{VO}_3$  (99.0%, Sigma-Aldrich) at  $80^\circ\text{C}$  for 4 h with vigorous stirring. The impregnated sample was dried at  $100^\circ\text{C}$  overnight and calcined in air at  $550^\circ\text{C}$  for 3 h at a ramp rate of  $5^\circ\text{C min}^{-1}$ . V surface density is used throughout the work, wherein the V loading [determined by ion-coupled plasma-optical emission spectroscopy (ICP-OES)] was normalized to the surface area of  $\text{In}_2\text{O}_3$  (Table S1). Catalysts were denoted as  $x\text{V}/\text{In}$ , wherein  $x$  represents the surface V density and varies from 0 to  $5.6 \text{ V nm}^{-2}$ .

**2.2. Activity Tests.** The following pre-mixed gas cylinders were purchased from airgas and used for activity tests, including 5%  $\text{C}_3\text{H}_8/\text{He}$  and 2%  $\text{CO}_2/\text{Ar}$ . The activity test of the  $\text{CO}_2$ -ODHP reaction was performed using an Altamira Instruments system (AMI-200). Typically, 100 mg of the catalyst was diluted with 600 mg of quartz sand (60–80 mesh). The mixture was loaded in a quartz U-tube (i.d. = 10 mm) with quartz wool at both ends of the mixture. Prior to the activity test, 2%  $\text{CO}_2/\text{Ar}$  was introduced to pretreat the catalyst at  $500^\circ\text{C}$  for 1 h under  $30 \text{ mL min}^{-1}$ . Then, the catalyst bed was cooled to the desired temperature. The activity test was initiated by switching to the reaction gas consisting of  $\text{C}_3\text{H}_8$ ,  $\text{CO}_2$  and balanced with  $\text{He}/\text{Ar}$  ( $\text{C}_3\text{H}_8/\text{CO}_2 = 1$ ) with weight hourly space velocity (WHSV) =  $18000 \text{ mL g}^{-1} \text{ h}^{-1}$ . The reaction was conducted in the temperature range of  $350$ – $540^\circ\text{C}$ , and each reaction temperature was maintained for 2 h.

Compositions of effluent gas were analyzed periodically using an online SRI 8610C gas chromatograph equipped with both thermal conductivity detector (TCD) and flame ionization detector (FID) detectors. MTX-WAX and Molecular Sieve 5A columns were attached to the TCD detector, analyzing CO and  $\text{CO}_2$ , while HayeSep-D and alumina were attached to the FID detector, analyzing hydrocarbons including  $\text{C}_3\text{H}_8$ ,  $\text{C}_3\text{H}_6$ ,  $\text{C}_2\text{H}_6$ ,  $\text{C}_2\text{H}_4$ , and  $\text{CH}_4$ . A mass spectrometer (Pfeiffer Vacuum) was also coupled with GC to monitor the real-time fragments of reactants and products in the effluent gas. Conversion and selectivity were calculated

based on the reported methods (see Section S3 in Supporting Information).<sup>39,40</sup>

To study the coking on spent catalysts, stability tests were run at 540 °C for ca. 10 h. The spent catalyst bed was flushed with Ar in 30 mL min<sup>-1</sup>, and the temperature was cooled to 50 °C. Then, the temperature-programmed oxidation (TPO) experiment was performed using either 2.5% O<sub>2</sub>/He or 2% CO<sub>2</sub>/Ar (40 mL min<sup>-1</sup>). The temperature was ramped up to 730 °C at a rate of 10 °C min<sup>-1</sup> and maintained for 0.5 h. The generated CO<sub>2</sub> or CO from the outlet was recorded by an OmniStar mass spectrometer (MS) (Pfeiffer Vacuum).

For kinetic studies, compositions were altered by varying the flow rates of 5% C<sub>3</sub>H<sub>8</sub>/He, 2% CO<sub>2</sub>/Ar, and Ar with a constant total flow rate of 40 mL min<sup>-1</sup>. All reactions were conducted at 500 °C where the conversion is below 10%, and the reduction of bulk In<sub>2</sub>O<sub>3</sub> is limited according to H<sub>2</sub>-temperature-programmed reduction (H<sub>2</sub>-TPR) results. Of note, all flow rates in the present work are normal temperature and pressure (NTP)-based.

**2.3. Characterization.** Elemental analysis was performed using ICP-OES on a PerkinElmer Avio 500 model instrument. The thermal stability of the catalysts was performed by TGA/DTG analysis using a TA Instruments SDT Q50 instrument. Prior to ramping up the temperature, each sample was pretreated with 25 mL min<sup>-1</sup> N<sub>2</sub> flow at 30–35 °C for 1 h to stabilize. Afterward, the sample was heated to 600 °C at a ramp rate of 5 °C min<sup>-1</sup> with 25 mL min<sup>-1</sup> N<sub>2</sub>. Such a process was recycled three times.

NH<sub>3</sub>-temperature-programmed desorption (TPD), CO<sub>2</sub>-TPD, and TPR were performed using AMI 200. ~50 mg of the fresh catalysts was charged into a U tube for all measurements, except V<sub>2</sub>O<sub>5</sub> (~40 mg) for H<sub>2</sub>-TPR. In NH<sub>3</sub>-TPD, the catalyst was pretreated in 2% CO<sub>2</sub>/Ar at 500 °C for 1 h. Then, the system was flushed in Ar, and the temperature was cooled to 120 °C. NH<sub>3</sub> adsorption (2% NH<sub>3</sub>/He) was carried out for 1 h (30 mL min<sup>-1</sup>), followed by Ar flush at 30 mL min<sup>-1</sup> for 1 h. TPD was then initiated from 120 to 730 °C (5 °C min<sup>-1</sup>) in Ar (30 mL min<sup>-1</sup>) and maintained for 0.5 h. In CO<sub>2</sub>-TPD, after similar pretreatment, CO<sub>2</sub> adsorption (2% CO<sub>2</sub>/Ar, 30 mL min<sup>-1</sup>) was performed at 140 °C for 1 h, followed by Ar flush and cooling to 50 °C. TPD was initiated from 50 to 620 °C (5 °C min<sup>-1</sup>) in Ar (30 mL min<sup>-1</sup>) and maintained for 0.5 h. In H<sub>2</sub>-TPR, the pretreated catalyst bed was cooled to 50 °C prior. Then, the catalyst was reduced in 4% H<sub>2</sub>/Ar (30 mL min<sup>-1</sup>) ramping from 50 to 830 °C (5 °C min<sup>-1</sup>) and maintained for 1 h. For both NH<sub>3</sub>- and CO<sub>2</sub>-TPD measurements, the effluent gas was recorded using the same mass spectrometer as TPO and activity tests. The TCD detector was used to record the H<sub>2</sub> signals, and a cooling trap was applied prior to the detector to trap moisture.

The NH<sub>3</sub> adsorption-DRIFTS experiment was performed using a Thermo Nicolet Nexus 670 FT-IR spectrometer with an MCT detector. Each spectrum was acquired with 32 scans at a resolution of 4 cm<sup>-1</sup>. The sample was loaded in a ceramic cup, and a DRIFTS cell (Pike Technologies) was used. In the experiment, the catalyst was pretreated at 500 °C in 2% CO<sub>2</sub>/Ar (30 mL min<sup>-1</sup>) for 1 h. The system was then cooled to 400, 300, and 200 °C in Ar (30 mL min<sup>-1</sup>), and corresponding spectra were collected as background references. The system was then cooled to 120 °C and flushed with Ar for 1 h. The NH<sub>3</sub> adsorption was performed at 120 °C using 1% NH<sub>3</sub>/Ar/He (30 mL min<sup>-1</sup>) for 30 min, followed by Ar flushing for 30 min (30 mL min<sup>-1</sup>) to remove physisorbed NH<sub>3</sub>. The

temperature was then heated up sequentially to 200, 300, and 400 °C at a ramp of 10 °C min<sup>-1</sup> in Ar. At each temperature, the spectra were continuously recorded every 30 s. The CO<sub>2</sub>-DRIFTS experiment was performed using the same equipment by following a similar procedure. 2% CO<sub>2</sub>/Ar was used during CO<sub>2</sub>-DRIFTS (30 mL min<sup>-1</sup>). The temperature was elevated to 200, 300, 400, 500, and 550 °C at a ramp of 10 °C min<sup>-1</sup>. The spectra were processed by using the background spectra acquired at corresponding temperatures.

The content and oxidation states of surface region VO<sub>x</sub> species were monitored by NAP-XPS. Spectra of the VO<sub>x</sub>-loaded In<sub>2</sub>O<sub>3</sub> catalyst were acquired with a SPECS DeviSim NAP reactor coupled with a PHOIBOS 150 NAP electron energy analyzer equipped with a XR 50 MF Al K $\alpha$  X-ray source (1486.7 eV). The sample was prepared by pressing the powder onto a SS 316 steel mesh by applying 5 MPa for 5 min. The pressed sample was then loaded onto a stainless-steel sample holder with a type K thermocouple enabling online measurement of the sample temperature as it was heated using an e-beam heater. The spectra were acquired with a 0.05 eV resolution and were repeated several times to reduce the noise-to-signal ratio. All gasses were flowed as to maintain a pressure of ~1 mbar in the NAP reaction cell. The resulting spectra were processed using CasaXPS (version 2.3.22PR1.0). Due to the lack of a strong C 1s spectra after the initial in situ oxidation of the catalyst, the O 1s spectra were used for binding energy correction. While some contribution by the VO<sub>x</sub> species existed, In<sub>2</sub>O<sub>3</sub> contributed the bulk of the O 1s signal, resulting in a reliable means of correction. The possible reduction of the In in the surface region was checked for by monitoring the In Auger spectra.<sup>41</sup> The V oxidation states were quantified by analyzing only the V 2p<sub>3/2</sub> spin-orbit split core spectra due to the weak intensity of the V 2p<sub>1/2</sub> spin-orbit split core spectra. Previously established binding energies, Lorentzian-Gaussian mixing ratios, and relative full width at half maximum (fwhm) values were applied for the V 2p<sub>3/2</sub> oxidation state quantification.<sup>42</sup> Consecutive treatments were carried out at 500 °C for 1 h at a time in the following sequence: 10% O<sub>2</sub>/Ar, 5% CO<sub>2</sub>/Ar, 2.5% C<sub>3</sub>H<sub>8</sub>/2.5% CO<sub>2</sub>/Ar, 5% CO<sub>2</sub>/Ar, and 5% C<sub>3</sub>H<sub>8</sub>/Ar. There is no regeneration between steps, and these measurements are continuous.

In situ Raman scattering for the samples under reaction conditions was collected on a multiwavelength Raman system using 532 nm laser excitation. Raman scattering was collected via a customized ellipsoidal mirror and diffracted by a fiber optics bundle to the spectrograph stage of a triple Raman spectroscopy (Princeton Instruments Acton Trivista 555). An edge filter (Semrock) was used in front of the UV-vis fiber optic bundle (Princeton instruments) to block the laser irradiation. A neutral density filter was used to attenuate the laser power to 20%, less than 10 mW at the sample position. An UV-enhanced liquid N<sub>2</sub>-cooled CCD detector (Princeton Instrument) was used to detect signals. The Raman catalytic reactor (Linkam CCR1000) was placed on an XY stage (Princeton Scientific, OptiScan XY system). During acquisition, the stage translates in a raster mode, which can provide the information of heterogeneity of the samples. The fast translation and the attenuated laser power are also able to minimize the laser damage of the sample. In the experiment, catalysts were pretreated in situ in the Raman reactor before Raman spectral collection at 120 °C. The pretreatment was carried out by heating the sample in 2% CO<sub>2</sub>/Ar (30 mL min<sup>-1</sup>) at 500 °C (ramping rate 10 °C min<sup>-1</sup>) and held for 30

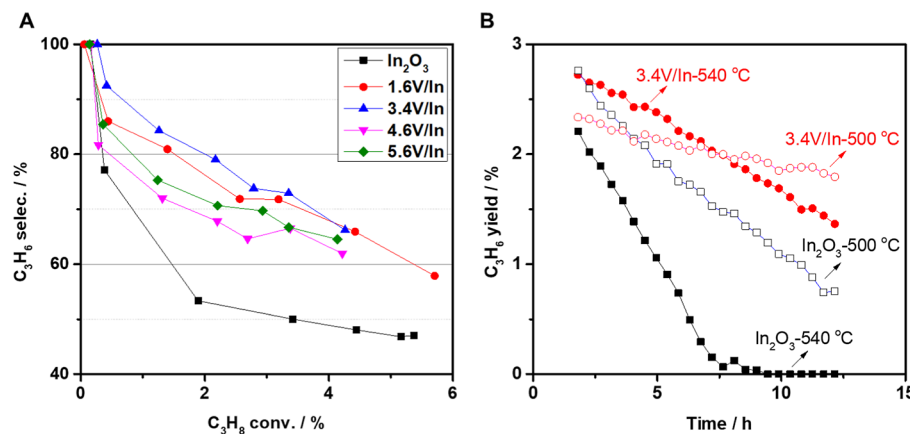


**Figure 1.** (A) Propylene selectivity–propane conversion plot over  $\text{VO}_x/\text{In}_2\text{O}_3$  catalysts with various surface V densities. Reaction conditions: 350–540 °C, ambient pressure,  $\text{C}_3\text{H}_8/\text{CO}_2 = 1$ , and WHSV = 18000 mL g<sup>-1</sup> h<sup>-1</sup>. (B) Stability on 3.4V/In and  $\text{In}_2\text{O}_3$  at 500 and 540 °C with similar WHSV and gas compositions.

min. In the reaction, the pretreated catalyst experienced consecutive treatments in  $\text{CO}_2$ ,  $\text{C}_3\text{H}_8/\text{CO}_2$  (1/1), and  $\text{CO}_2$  again at 500 °C. The Raman spectra of dehydrated catalysts were acquired at a different Raman system, and the detailed procedures are described in the [Supporting Information](#).

UV-vis DRS measurements were performed in the 200–800 nm range with an Agilent Cary 5000 UV-vis and NIR spectrophotometer. Polytetrafluoroethylene powder (35 μm, Sigma-Aldrich) was used as a reflectance standard.  $\text{VO}_x/\text{In}_2\text{O}_3$  catalysts were thoroughly mixed with silica at a 1:1 weight ratio to overcome the sample's signal nonlinearity with intensity. Fumed silica (Cab-O-Sil EH-5, Cabot) was first hydrated with Milli-Q ultrapure water and then dried under 100 mL min<sup>-1</sup> of dry air (AI D300, Airgas) for 16 h. A heating/cooling rate of 10 °C min<sup>-1</sup> was used throughout. After crushing with an agate mortar and pestle, the silica was calcined at 500 °C for 4 h under 100 mL min<sup>-1</sup> of air. The silica-diluted  $\text{VO}_x/\text{In}_2\text{O}_3$  samples were loaded into a reaction cell (Harrick Scientific HVC-DR2) and connected to a gas flow control system. A Harrick ATC temperature controller unit controlled the catalyst temperature. Dehydration was performed under 10% O<sub>2</sub>/Ar (airgas, 30 mL min<sup>-1</sup>) as samples were heated to 500 °C and held for 30 min, followed by cooling to 120 °C where the dehydrated spectra were taken. The spectra were acquired with 1 nm resolution and a dwell time of 1.5 s (a scan rate of 40 nm min<sup>-1</sup>) while using a double beam mode with full slit height and a slit beam width of 2 nm. The surface  $\text{VO}_x$  direct band gap was determined using the Kubelka–Munk formalism to convert the reflectance into the equivalent absorption coefficient function,  $F(R_\infty)$ , where  $R_\infty$  is the ratio of the sample reflectance to the standard reflectance. The respective edge energies of the dehydrated V<sup>5+</sup> molecular structures were calculated from the linear fit intercept of a plot of  $(F(R_\infty)\hbar\nu)^2$  as a function of the photon energy ( $\hbar\nu$ ) on the linear low-energy side of the plot (errors are usually estimated to be ~0.11 eV<sup>43</sup>). The direct band gap energy is assumed to have an absolute error lower than 0.11 eV related to the inherent uncertainty in the manual fitting process.<sup>43</sup>

XAS measurements were conducted at the materials research collaborative access team bending magnet line (10-BM) of the advanced photon source, Argonne National Laboratory.<sup>44</sup> Measurements at the V K edge (5465 eV) were performed in the fluorescence mode using a vortex four-element detector. The sample wafer and fluorescence detector were positioned

45 and 90° relative to the X-ray beam respectively. Fluorescence-mode samples were ground into a fine powder in a mortar and pestle and pressed into a self-supporting wafer inside a stainless-steel sample holder. The potential for over-absorption artifacts was assessed by estimating the transmission edge step at the V K edge of three absorption lengths worth of sample. The calculated edge step for each sample composition was found to be well below 0.1, meaning over-absorption artifacts are negligibly small for the fluorescence data. In situ treatments were performed in a heated reaction cell described previously.<sup>45</sup> The sample temperature was monitored using a K-type thermocouple, and gas was introduced using a set of mass flow controllers. He, CO<sub>2</sub>, and 5% propane in He were acquired from airgas (ultra-high purity grade). Samples were measured as-synthesized and after a sequence of four treatments in  $\text{CO}_2$  and  $\text{C}_3\text{H}_8/\text{CO}_2$ , followed by in  $\text{C}_3\text{H}_8$ , and  $\text{CO}_2$  after the reaction. After each treatment, the sample was cooled to room temperature in the treatment atmosphere, and spectra were collected under 100 sccm of the flowing gas. A total of six scans were collected for each treatment and averaged to yield the final data set. No discernible changes were observed between scans for a given treatment. Detailed experimental description and data analysis can be found in the [Supporting Information](#).

### 3. RESULTS AND DISCUSSION

**3.1. Activity Performance.** To evaluate the reactivity of  $\text{VO}_x/\text{In}_2\text{O}_3$  catalysts, the  $\text{CO}_2$ -ODHP reaction was conducted in the temperature range of 350–540 °C. A blank test was performed on quartz sand under the same reaction conditions, and no activity was observed ([Figure S2](#)). As shown in [Figure 1A](#),  $\text{In}_2\text{O}_3$  shows a high  $\text{C}_3\text{H}_6$  selectivity at a lower  $\text{C}_3\text{H}_8$  conversion, but the selectivity decreases rapidly with the increasing conversion. All  $\text{VO}_x$ -loaded catalysts present a higher  $\text{C}_3\text{H}_6$  selectivity than  $\text{In}_2\text{O}_3$  under isoconversional conditions, and 3.4V/In exhibits the highest  $\text{C}_3\text{H}_6$  selectivity among all  $\text{VO}_x/\text{In}_2\text{O}_3$  catalysts. For example, at 3.3%  $\text{C}_3\text{H}_8$  conversion, the  $\text{C}_3\text{H}_6$  selectivity of 3.4V/In is 73%, which is ca. 1.5-fold higher than that of  $\text{In}_2\text{O}_3$ . Moreover, 3.4V/In exhibits well-improved stability in comparison to  $\text{In}_2\text{O}_3$  at both 500 and 540 °C within the examined time-on-stream (TOS) ([Figure 1B](#)). The reduction in  $\text{C}_3\text{H}_6$  yield is mostly related to the decrease in conversion (deactivation) but not the decrease in selectivity.  $\text{C}_3\text{H}_8$  conversion decreases with the addition of

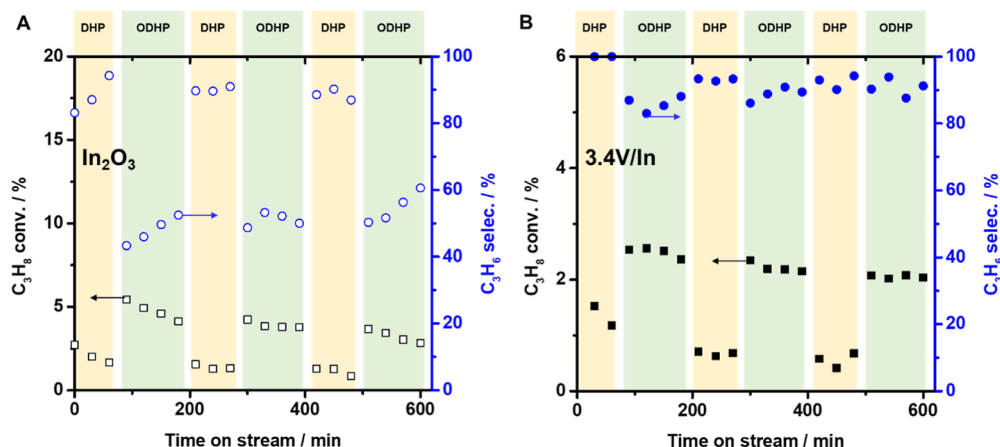


**Figure 2.** Catalytic performance of comparative studies between DHP and CO<sub>2</sub>-ODHP on In<sub>2</sub>O<sub>3</sub> (A) and 3.4V/In (B). The reaction was conducted at 500 °C. For both DHP and CO<sub>2</sub>-ODHP, C<sub>3</sub>H<sub>8</sub> composition was fixed at 1.4%, and WHSV was 18000 mL g<sup>-1</sup> h<sup>-1</sup>. In CO<sub>2</sub>-ODHP, the C<sub>3</sub>H<sub>8</sub>/CO<sub>2</sub> ratio was 1/1.

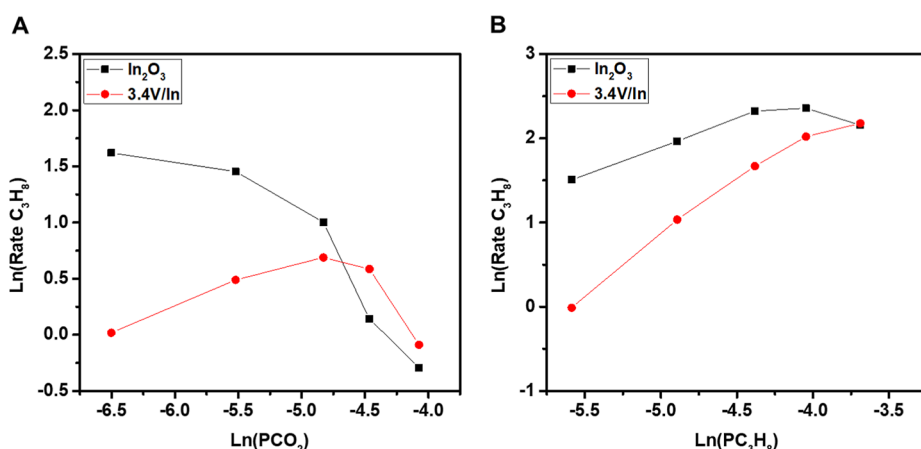


**Figure 3.** Effect of CO<sub>2</sub> (A) and C<sub>3</sub>H<sub>8</sub> (B) compositions on the C<sub>3</sub>H<sub>8</sub> conversion rate over 3.4V/In and In<sub>2</sub>O<sub>3</sub>. Compositions were altered by varying the flow rates of 5% C<sub>3</sub>H<sub>8</sub>/He, 2% CO<sub>2</sub>/Ar, and Ar with a constant total flow rate of 40 mL min<sup>-1</sup>. Compositions of C<sub>3</sub>H<sub>8</sub> and CO<sub>2</sub> were fixed at 0.8 and 1.0% for (A) and (B), respectively. All reactions were conducted at 500 °C where the conversion is below 10%, and the reduction of bulk In<sub>2</sub>O<sub>3</sub> is limited according to H<sub>2</sub>-TPR results.

VO<sub>x</sub>, and this is even more distinct in the trend of CO<sub>2</sub> conversion (Figure S3).

To study the role of CO<sub>2</sub> in the reaction paths, comparative studies between DHP and CO<sub>2</sub>-ODHP were performed on 3.4V/In and In<sub>2</sub>O<sub>3</sub>. As shown in Figure 2A, In<sub>2</sub>O<sub>3</sub> presents a relatively lower C<sub>3</sub>H<sub>8</sub> conversion (ca. 2%) but a higher C<sub>3</sub>H<sub>6</sub> selectivity (ca. 90%) under DHP conditions. Introducing CO<sub>2</sub> results in a significant reduction in selectivity to ca. 50%, while the C<sub>3</sub>H<sub>8</sub> conversion is almost doubled. Differently, the selectivity of 3.4V/In is well retained in the presence of CO<sub>2</sub>, together with a nearly doubled conversion (Figure 2B). The formation rate of products is also evaluated in space-time-yield (STY), as shown in Figure S4. 3.4V/In shows a comparable C<sub>3</sub>H<sub>6</sub> STY as In<sub>2</sub>O<sub>3</sub> during CO<sub>2</sub>-ODHP cycles and even surpasses In<sub>2</sub>O<sub>3</sub> during the third cycle of CO<sub>2</sub>-ODHP (Figure S4A). On the other hand, the presence of CO<sub>2</sub> during CO<sub>2</sub>-ODHP significantly promotes the formation of CO on In<sub>2</sub>O<sub>3</sub> in comparison to 3.4V/In (Figure S4B). Apparently, CO<sub>2</sub> plays a positive role in promoting the dehydrogenation reaction in the presence of VO<sub>x</sub>. The CO<sub>2</sub>-based CO selectivity was tracked to study the carbon source of formed CO. For both RWGS and CO<sub>2</sub>-ODHP, the stoichiometry gives a 1/1 M ratio between consumed CO<sub>2</sub> and formed CO, while that ratio

is 1/2 for PDR. As shown in Figure S5, both In<sub>2</sub>O<sub>3</sub> and 3.4V/In exhibit a CO selectivity beyond 100%, implying the contribution of PDR in CO formation other than CO<sub>2</sub>-ODHP. In<sub>2</sub>O<sub>3</sub> presents an appreciably higher value (130–140%) than 3.4V/In (110–120%) under isoconversional conditions (Figure S5). In other words, 30–40% of CO originates from PDR on In<sub>2</sub>O<sub>3</sub>, while that has been decreased to 10–20% from PDR on 3.4V/In. In addition, the relationship between the CO/C<sub>3</sub>H<sub>6</sub> molar ratio and CO<sub>2</sub>/C<sub>3</sub>H<sub>8</sub> conversion ratio of three cycles of CO<sub>2</sub>-ODHP is plotted in Figure S6. Of note, the stoichiometries of CO<sub>2</sub>-ODHP and PDR suggest 1/1 and 3/1 M ratios, respectively. As shown in Figure S6, the CO<sub>2</sub>/C<sub>3</sub>H<sub>8</sub> conversion ratio is higher than 1/1 for both In<sub>2</sub>O<sub>3</sub> and 3.4V/In, again indicating the occurrence of PDR. On the other hand, 3.4V/In presents a drastically lower CO/C<sub>3</sub>H<sub>6</sub> molar ratio than In<sub>2</sub>O<sub>3</sub>, clearly demonstrating a shift in reaction pathways from PDR to CO<sub>2</sub>-ODHP. Such a shift in reaction paths can also be reflected from mass spectrometer (MS) signals of H<sub>2</sub>. As shown in Figure S7, In<sub>2</sub>O<sub>3</sub> shows significantly higher H<sub>2</sub> signals (*m/z* = 2) than 3.4V/In during each ODHP cycle of DHP-ODHP alternating experiments. Such a distinction also signifies the VO<sub>x</sub>-induced shift in reaction pathways as PDR produces much more H<sub>2</sub> than ODHP based

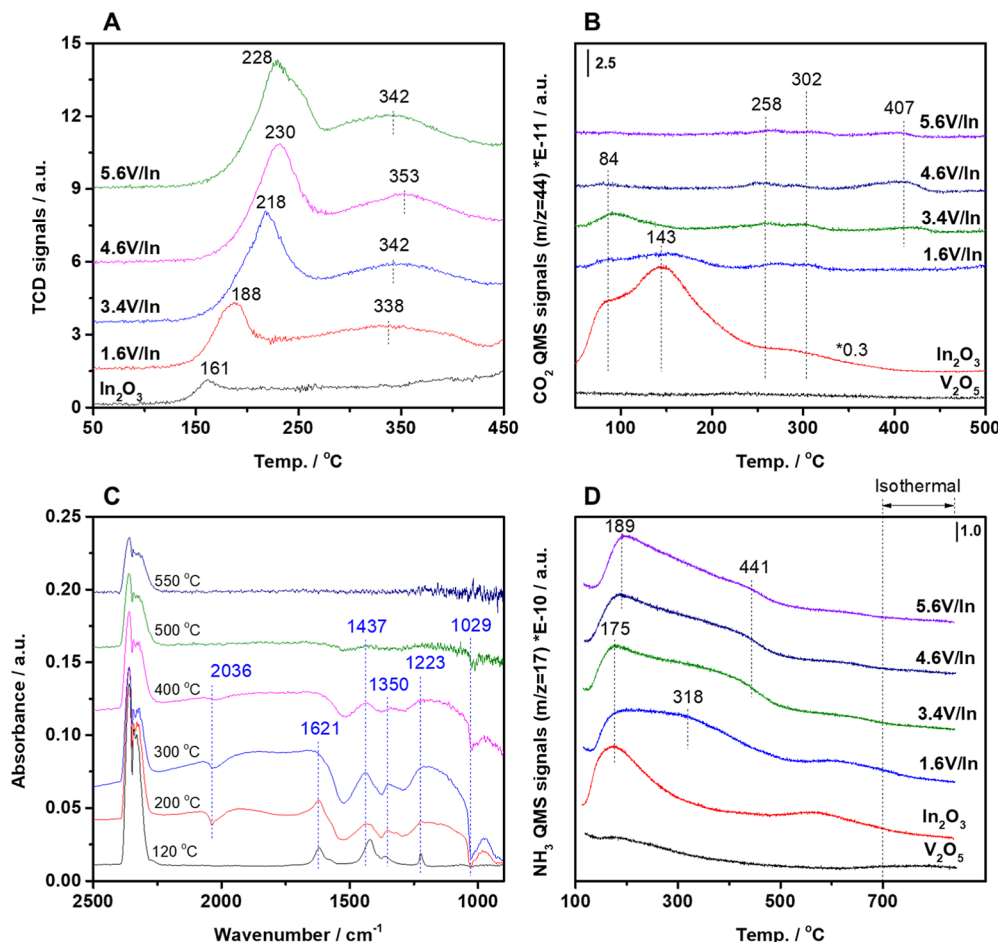


**Figure 4.** Reducibility and acid–base properties of  $\text{VO}_x/\text{In}_2\text{O}_3$  catalysts.  $\text{H}_2$ -TPR (A),  $\text{CO}_2$ -TPD (B),  $\text{CO}_2$ -DRIFTS spectra of 3.4V/In (C), and  $\text{NH}_3$ -TPD (D) profiles for all catalysts and references.

on stoichiometry. It is further speculated that combining  $\text{In}_2\text{O}_3$  with redox-active  $\text{VO}_x$  enables the modification of surface active sites, which leads to such a shift from PDR to  $\text{CO}_2$ -ODHP. This will be majorly explored by characterizations, which will be discussed in the following sections.

As aforementioned,  $\text{CO}_2$ -ODHP can proceed through two mechanisms. The first scenario includes a net reaction of DHP and RWGS, which can be linked by the  $\text{H}_2$  produced from DHP and then consumed by RWGS.<sup>11,29</sup> The other is a one-cycle mechanism, in which  $\text{CO}_2$  closes the cycle to form CO without going through a separate RWGS step.<sup>29</sup> To provide insights into the reaction mechanisms in the presence and absence of  $\text{VO}_x$  on  $\text{In}_2\text{O}_3$ , RWGS activity tests were performed on  $\text{In}_2\text{O}_3$  and 3.4V/In, and the temperature-dependent  $\text{H}_2$  and  $\text{CO}_2$  conversions are plotted in Figure S8. Both catalysts present only RWGS activity without any detectable methanation activity. 3.4V/In shows slightly lower conversions in both reagents than  $\text{In}_2\text{O}_3$ , especially at higher temperatures. Clearly, incorporating  $\text{VO}_x$  barely impacts the reaction pathway of RWGS but only activity. This suggests that the lower  $\text{H}_2$  amount detected during  $\text{CO}_2$ -ODHP over  $\text{VO}_x/\text{In}_2\text{O}_3$  than  $\text{In}_2\text{O}_3$  is not because of the extensive RWGS consumption but rather related to less  $\text{H}_2$  production from the reactions including PDR and  $\text{CO}_2$ -ODHP. Thus, it is reasonable to deduce that the one-cycle mechanism contributes more to  $\text{CO}_2$ -ODHP on  $\text{VO}_x/\text{In}_2\text{O}_3$ .

Arrhenius plots and apparent activation energy ( $E_{\text{app}}$ ) over 3.4V/In and  $\text{In}_2\text{O}_3$  are present in Figure S9 and Table S3, respectively. Adding  $\text{VO}_x$  reduces  $E_{\text{app}}$  of  $\text{C}_3\text{H}_8$  from 108.5 kJ mol<sup>-1</sup> of  $\text{In}_2\text{O}_3$  to 87.6 kJ mol<sup>-1</sup> of 3.4V/In. This might be associated with a pathway shift from PDR to  $\text{CO}_2$ -ODHP. Kinetics studies were then conducted on the same catalysts to examine the influence of reactant compositions on reactivity. As shown in Figure 3A, the  $\text{C}_3\text{H}_8$  conversion rate declines monotonically with the increase in  $\text{CO}_2$  compositions. As a more acidic molecule,  $\text{CO}_2$  adsorption is more favorable than  $\text{C}_3\text{H}_8$  on  $\text{In}_2\text{O}_3$ , exerting negative impacts on propane dehydrogenation.<sup>28</sup> Differently, the conversion rate for 3.4V/In shows a volcano-like shape with the increase in  $\text{CO}_2$  compositions. The presence of  $\text{VO}_x$  likely alleviates the competitive adsorption of reagent molecules at relatively lower  $\text{CO}_2$  compositions (Figure 3A). This can also be associated with the  $\text{VO}_x$ -induced shift of the reaction pathway from PDR to  $\text{CO}_2$ -ODHP. Although the competition still governs at higher  $\text{CO}_2$  compositions, the activity of 3.4V/In starts to surpass that of  $\text{In}_2\text{O}_3$ . As shown in Figure 3B, the competitive adsorption of reagent molecules still occurs on  $\text{In}_2\text{O}_3$ , while that is not evident on 3.4V/In.

To evaluate coking, TPO experiments were conducted on spent catalysts by using both  $\text{O}_2$  and  $\text{CO}_2$  as oxidants. As shown in Figure S10A and Table S2, the peak of formed  $\text{CO}_2$  shifts toward lower temperatures for 3.4V/In in comparison to  $\text{In}_2\text{O}_3$ ; a reduced amount of formed  $\text{CO}_2$  from  $\text{O}_2$ -TPO

**Table 1.** Physicochemical Properties and Characterization Results of  $\text{VO}_x/\text{In}_2\text{O}_3$  Catalysts and  $\text{In}_2\text{O}_3$  and  $\text{V}_2\text{O}_5$ 

| catalyst                | $\text{H}_2$ consumption from $\text{H}_2$ -TPR |                                      | ads. $\text{CO}_2$ amt. from $\text{CO}_2$ -TPD/ $\mu\text{mol g}^{-1}$ | ads. $\text{NH}_3$ amt. from $\text{NH}_3$ -TPD/ $\mu\text{mol g}^{-1}$ |
|-------------------------|---|--------------------------------------|---|---|
|                         | $\text{In}_2\text{O}_3^a/\mu\text{mol g}^{-1}$  | $\text{VO}_x^b/\mu\text{mol g}^{-1}$ |   |   |
| $\text{In}_2\text{O}_3$ | 34.5  |                                      | 96.6  | 217.5   |
| $\text{V}_2\text{O}_5$  |   |                                      | 0.9   | 14.0  |
| 1.6V/In                 | 134.9   | 130.0                                | 3.5   | 265.5   |
| 3.4V/In                 | 351.4   | 288.7                                | 3.1   | 292.0   |
| 4.6V/In                 | 398.9   | 305.4                                | 2.1   | 278.8   |
| 5.6V/In                 | 426.4   | 379.9                                | 1.3   | 262.5   |

<sup>a</sup>Quantified based on the reduction peak ranging from ca. 160 to 230 °C. <sup>b</sup>Quantified based on the reduction peak at 340–350 °C.

profiles is observed on 3.4V/In than  $\text{In}_2\text{O}_3$ . The presence of  $\text{VO}_x$  facilitates the coke removal and resists coking. The  $\text{CO}_2$ -TPO profile confirms the formation of CO at ca. 396 °C (Figure S10B,C). The reverse Boudouard reaction likely occurs for coke removal during  $\text{CO}_2$ -ODHP.

In sum, incorporating  $\text{VO}_x$  into  $\text{In}_2\text{O}_3$  improves the  $\text{C}_3\text{H}_6$  selectivity and improved stability. Kinetic studies imply that  $\text{VO}_x$  plays an important role in governing the reaction pathway via propane dehydrogenation instead of PDR on  $\text{In}_2\text{O}_3$  in the presence of  $\text{CO}_2$ . Whether these catalytic behaviors originate from the individual materials and/or in a cooperative fashion between  $\text{VO}_x$  and  $\text{In}_2\text{O}_3$  is of interest to explore in the next step, especially their correlations with surface acid–base properties and redox cycles. For this purpose, the catalysts were characterized by various techniques, and the results will be discussed in the following sections.

**3.2. Reducibility and Acid–Base Properties.** **3.2.1. Reducibility.** Reducibility of catalysts was studied by  $\text{H}_2$ -TPR, and the resulting profiles are shown in Figure 4A.  $\text{In}_2\text{O}_3$  exhibits a peak at 161 °C, corresponding to the reduction of In oxide species with smaller particle sizes.<sup>25,34,46,47</sup> With the increase in V loadings, this peak gradually shifts to higher temperatures, especially from 1.6 to 3.4V nm<sup>-2</sup>, beyond which the shift becomes less significant. Clearly, these reducible  $\text{In}_2\text{O}_3$  species represent the ones that have intimate interactions with  $\text{VO}_x$ . A subpeak appears at 340–350 °C, which can be attributed to the reduction of  $\text{VO}_x$  species.<sup>48</sup> Considering the reduction peaks of bulk  $\text{V}_2\text{O}_5$  (660–700 °C, Figure S11), these  $\text{VO}_x$  species are dispersed on  $\text{In}_2\text{O}_3$ . These reducible  $\text{VO}_x$  species increase significantly from 130.0  $\mu\text{mol g}^{-1}$  at 1.6V/In to 288.7  $\mu\text{mol g}^{-1}$  at 3.4V/In, beyond which its increase becomes slow (Table 1). A similar trend can be evidenced from the increase in the reducible  $\text{In}_2\text{O}_3$  species ranging from 160 to 230 °C. It suggests that 3.4V nm<sup>-2</sup> is approaching a monolayer surface coverage, which might be associated with a higher  $\text{C}_3\text{H}_6$  selectivity for 1.6V/In and 3.4V/In.<sup>1</sup> The reduction of bulk  $\text{In}_2\text{O}_3$  starts from ca. 500 °C and presents a maximum peak at ca. 751 °C (Figure S11) for  $\text{In}_2\text{O}_3$ . Incorporating  $\text{VO}_x$  into  $\text{In}_2\text{O}_3$  shifts the reduction of bulk  $\text{In}_2\text{O}_3$  toward higher temperatures, indicating its role in inhibiting the deep reduction of  $\text{In}_2\text{O}_3$  (Figure S11). Considering the lower propylene selectivity and yield and poorer stability at higher temperatures of  $\text{In}_2\text{O}_3$  (Figure 1), it is suggested that the deep reduction of  $\text{In}_2\text{O}_3$  has a negative impact on the catalytic performance and stability.

**3.2.2. Basicity.** To study the surface basicity,  $\text{CO}_2$ -TPD measurements were performed. Resultant profiles are present in Figure 4B, along with quantified  $\text{CO}_2$  amount in Table 1. For reference materials,  $\text{V}_2\text{O}_5$  hardly exhibits  $\text{CO}_2$  adsorption, while  $\text{In}_2\text{O}_3$  shows a significantly high adsorption capacity (96.6  $\mu\text{mol g}^{-1}$ ). On  $\text{In}_2\text{O}_3$ , the desorption peak within ca. 50–

300 °C can be attributed to adsorbed  $\text{CO}_2$  on thermal-induced oxygen vacancies.<sup>36,49</sup>  $\text{CO}_2$ -DRIFTS spectra show that  $\text{CO}_2$  is adsorbed as carbonate and bicarbonate on  $\text{In}_2\text{O}_3$  (Figure S12 and Table S4).<sup>50–52</sup> In addition to oxygen vacancies, the surface hydroxyl groups also play a role in  $\text{CO}_2$  adsorption, the consumption of which is evident from DRIFTS spectra (Figure S13A). The presence of  $\text{VO}_x$  considerably reduces the  $\text{CO}_2$  adsorption capacity, especially the weakly bonded species, while retaining parts of the medium-bonded species (Figure 4B). Carbonate and bicarbonate are still evident on 3.4V/In through DRIFTS (Figure 4C and Table S5), except that the peak intensities are notably lower than those observed on  $\text{In}_2\text{O}_3$  alone, again corroborating the suppression of  $\text{CO}_2$  adsorption after incorporating  $\text{VO}_x$ . This is likely linked to the inhibited formation of surface oxygen vacancies and consumed hydroxyl groups by anchoring  $\text{VO}_x$  (Figure S13B). Two negative IR bands, centered at 1029 and 2036  $\text{cm}^{-1}$ , appear on 3.4V/In (Figure 4C), which correspond to the fundamental stretching vibration and the overtone of vanadyl groups ( $\text{V}=\text{O}$ ), respectively.<sup>53–55</sup> The negative bands are indicative of the  $\text{CO}_2$  adsorption on vanadyl groups.<sup>56</sup> In sum, adding  $\text{VO}_x$  significantly neutralizes the surface basicity of  $\text{In}_2\text{O}_3$ . Together with the retarded reduction of  $\text{In}_2\text{O}_3$ , the presence of  $\text{VO}_x$  might explain the suppressed PDR pathway.

**3.2.3. Acidity.** The surface acidity of the dehydrated  $\text{VO}_x/\text{In}_2\text{O}_3$  catalysts was probed by  $\text{NH}_3$ -TPD, and the resulting profiles are shown in Figure 4D.  $\text{In}_2\text{O}_3$  presents a major peak at ca. 175 °C with a wide range, as well as another bump at ca. 600 °C. Incorporating  $\text{VO}_x$  results in an extra peak at ca. 320–440 °C, the position of which gradually shifts to higher temperatures with the increase in V loadings. Meanwhile, the bump observed on  $\text{In}_2\text{O}_3$  at ca. 600 °C diminishes. All  $\text{VO}_x/\text{In}_2\text{O}_3$  catalysts exhibit a higher  $\text{NH}_3$  adsorption capacity than  $\text{In}_2\text{O}_3$  (Table 1).  $\text{VO}_x$  is known with its acid sites such as vanadyl groups ( $\text{V}=\text{O}$ ).<sup>1</sup> Adding  $\text{VO}_x$  can increase the surface acid sites below or close to a monolayer-surface coverage.

The acid sites were further studied by *in situ* DRIFTS.  $\text{In}_2\text{O}_3$  exhibits both Lewis ( $\text{NH}_3$  species bands at 1622  $\text{cm}^{-1}$ ) and Brønsted bands ( $\text{NH}_4^+$  species at 1407 to 1434  $\text{cm}^{-1}$ ), as shown in Figure S14A. The adsorbed  $\text{NH}_3$  on Lewis acid sites is less thermally stable than that on Brønsted acid sites as it diminishes below 300 °C. Thus, the peak at ca. 175 °C from TPD profiles (Figure 4D) signifies the  $\text{NH}_3$  adsorption on Lewis acid sites of  $\text{In}_2\text{O}_3$ , while the bump at ca. 600 °C is indicative of the  $\text{NH}_3$  adsorption on Brønsted acid sites such as hydroxyl groups. Both Lewis and Brønsted acid sites are also observed on 3.4V/In from Figure S14B. Except for the remaining Lewis sites on  $\text{In}_2\text{O}_3$  responsible for the low-temperature desorption peak (~175–190 °C) from the TPD profile (Figure 4D), the  $\text{VO}_x$ -dependent peaks at ca. 320–440 °C (Figure 4D) correspond to the acid sites that are associated

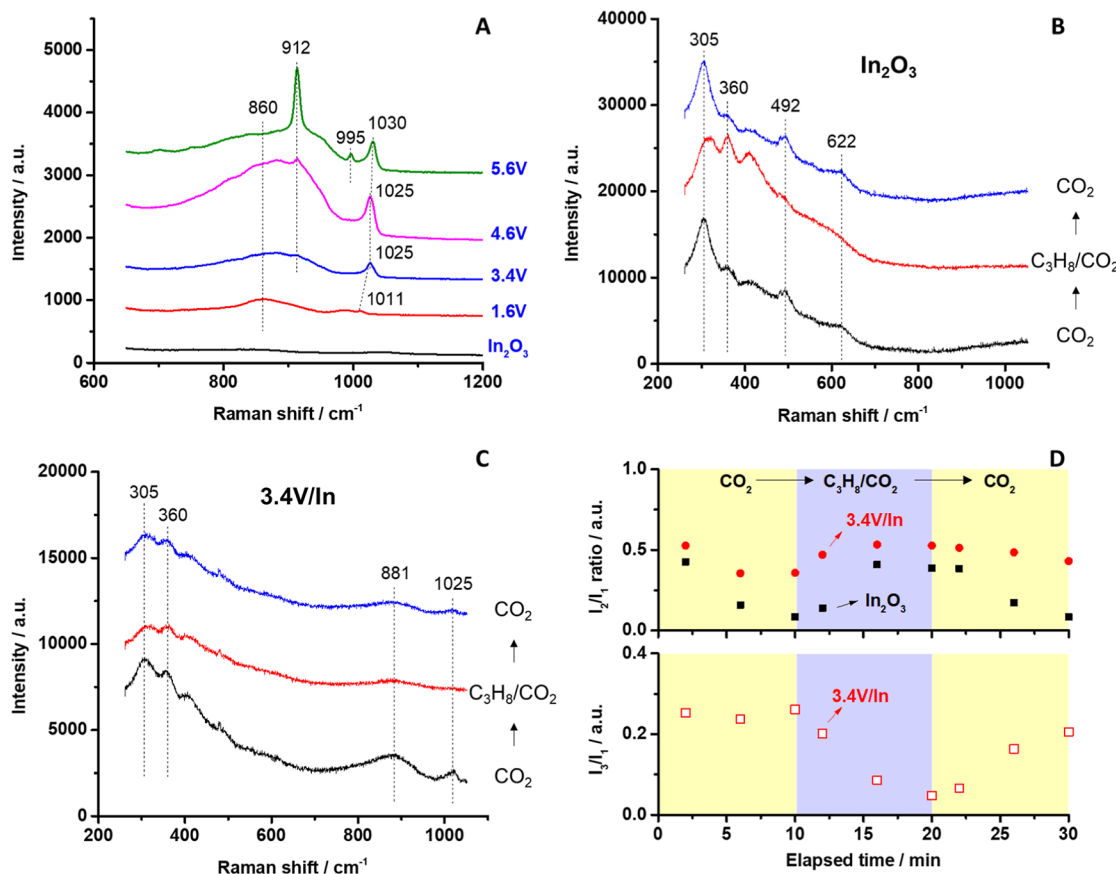


**Figure 5.** In situ Raman spectra of dehydrated catalysts (A), in situ Raman spectra of In<sub>2</sub>O<sub>3</sub> (B) and 3.4V/In (C) under reaction conditions at 500 °C by following the sequence of CO<sub>2</sub> → C<sub>3</sub>H<sub>8</sub>/CO<sub>2</sub> → CO<sub>2</sub> with 10 min for each condition. (D) Variations in I<sub>2</sub>/I<sub>1</sub> and I<sub>3</sub>/I<sub>1</sub> ratios as a function of TOS under switch-mode experiments based on (B,C). I<sub>1</sub>: area of the peak at 305 cm<sup>-1</sup>, I<sub>2</sub>: area of the peak at 360 cm<sup>-1</sup>, and I<sub>3</sub>: area of the peak at 1025 cm<sup>-1</sup>.

with VO<sub>x</sub> species, such as vanadyl groups and/or bridging hydroxyl groups (V=O(H)-In). Two negative bands, centered at 1024 and 2031 cm<sup>-1</sup>, emerge upon NH<sub>3</sub> adsorption (Figure S14B), corresponding to the consumption of vanadyl groups of VO<sub>x</sub> due to the interaction with NH<sub>3</sub>.<sup>1,55</sup> The negative peak becomes less intense with the desorption temperature of NH<sub>3</sub> and almost disappears after 400 °C desorption, suggesting that the surface VO<sub>x</sub> species on In<sub>2</sub>O<sub>3</sub> at below or close to a monolayer coverage are responsible for the medium strength (below 400 °C in Figure 4D) acid sites.

**3.3. Catalyst Structure and Redox Cycle. 3.3.1. Catalyst Structure.** Figure 5A shows the Raman spectra of all dehydrated VO<sub>x</sub>/In<sub>2</sub>O<sub>3</sub> catalysts at 120 °C in O<sub>2</sub>/Ar after the pretreatment at 500 °C. For 1.6V/In, the band at 1011 cm<sup>-1</sup>, corresponding to the vanadyl groups,<sup>55</sup> signifies the presence of less polymerized vanadates such as monovanadate. With the increase in VO<sub>x</sub> loadings, the band gradually shifts to 1025 cm<sup>-1</sup> and finally to 1030 cm<sup>-1</sup>, demonstrating the progressive formation of polyvanadate on the catalyst surface. A broad peak, centered at ca. 860 cm<sup>-1</sup>, emerges on all VO<sub>x</sub>/In<sub>2</sub>O<sub>3</sub> catalysts, indicating the presence of In-O-V structure in the catalyst.<sup>1,55</sup> The other V-involving species include the stretching vibration of V=O for V<sub>2</sub>O<sub>5</sub> particles at 995 cm<sup>-1</sup> for 5.6V/In (Figure S1) and the symmetric stretching vibration of VO<sub>4</sub><sup>3-</sup> in InVO<sub>4</sub> at 912 cm<sup>-1</sup> for 3.4–5.6V/In catalysts.<sup>1,55,57–59</sup> The Raman cross section of V<sub>2</sub>O<sub>5</sub> is 10 times larger than dispersed VO<sub>x</sub> species.<sup>60</sup> Based on the peak intensities in Figure 5A, dispersed VO<sub>x</sub> is dominant. Among

these species, mono- and polyvanadates have been demonstrated as active sites for the ODHP reaction, while V<sub>2</sub>O<sub>5</sub> particles lead to over-oxidation.<sup>1,27</sup>

UV-vis DRS measurements were performed to verify the structure of vanadate at the surface. The Tauc plots for VO<sub>x</sub>/In<sub>2</sub>O<sub>3</sub> catalysts are presented in Figure S15. The edge energies of the ligand-to-metal-charge-transfer transitions of the dehydrated V<sup>5+</sup> molecular structures were calculated from the abscissa intercept of the photon energy in the low-energy side of the in situ UV-vis DRS-derived Tauc plots. The increasing addition of vanadium to In<sub>2</sub>O<sub>3</sub> initially results in a decrease in the edge energy from 3.13 (1.6V/In) to 2.95 eV (3.4V/In), indicating an increase in the polymerization degree of surface VO<sub>x</sub> site. This suggests that at the lowest vanadium loading (1.6V/In), the surface VO<sub>x</sub> species are a mix of monomeric (~20%) and polymeric (~80%) VO<sub>4</sub> sites.<sup>61</sup> At higher vanadium loadings, the edge energy first decreases to 2.95 eV (3.4V/In) and then increases slightly to ~3.00 eV for both 4.6 and 5.6V/In, indicative of completely polymeric VO<sub>4</sub> surface sites.<sup>61</sup> In sum, VO<sub>x</sub> surface species polymerize progressively on In<sub>2</sub>O<sub>3</sub> with loadings, with only a limited fraction of monomeric sites (~20%) present at a low surface V density of 1.6V. These observations are in general consistent with the Raman results.

In situ Raman experiments were performed to study the catalyst structures under reaction conditions. As shown in Figure 5B, In<sub>2</sub>O<sub>3</sub> presents four major bands. The Raman feature at 305 cm<sup>-1</sup> is interpreted as the δ(InO<sub>6</sub>) bending

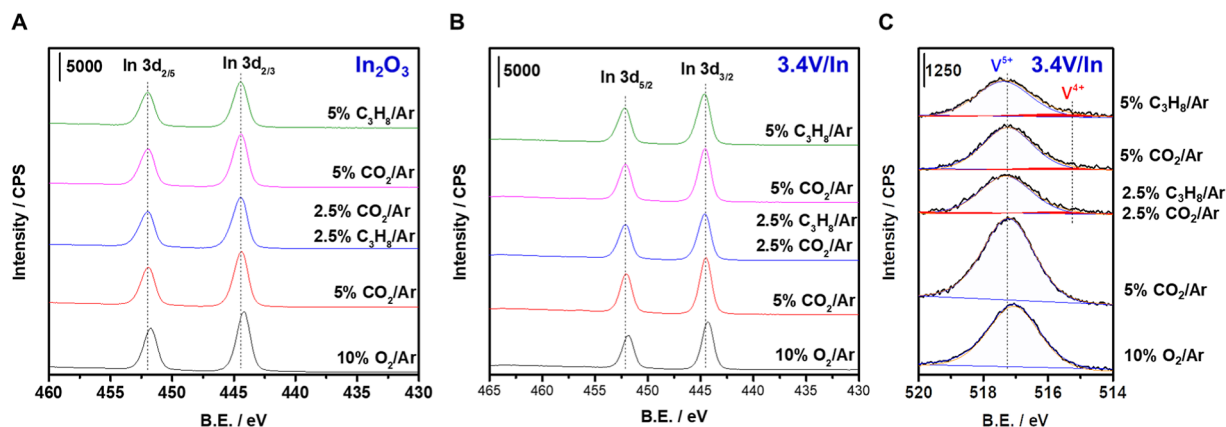


**Figure 6.** In situ In 3d NAP-XPS spectra of  $\text{In}_2\text{O}_3$  (A) and 3.4V/In (B) and V 2p<sub>3/2</sub> XPS spectra of 3.4V/In (C) under consecutive treatments in  $\text{O}_2$ ,  $\text{CO}_2$ ,  $\text{C}_3\text{H}_8/\text{CO}_2$ , and  $\text{CO}_2$  again after the reaction for regeneration and  $\text{C}_3\text{H}_8$  at 500 °C.

vibration of octahedra of *bcc*- $\text{In}_2\text{O}_3$ ; the band at 360  $\text{cm}^{-1}$  is assigned to the  $\nu(\text{In}-\text{O}-\text{In})$  stretching vibration of  $\text{In}-\text{O}-\text{In}$  linkage; the other two bands at 492 and 622  $\text{cm}^{-1}$  correspond to the stretching vibrations of the same  $\nu(\text{InO}_6)$  octahedra.<sup>36,49,62–64</sup> By switching from  $\text{CO}_2$  to  $\text{C}_3\text{H}_8/\text{CO}_2$ , the relative intensity of 360  $\text{cm}^{-1}$  increases and subsequently decreases after switching back to  $\text{CO}_2$ . In contrast, such a change is not significant on 3.4V/In under the same conditions (Figure 5C). The band at 360  $\text{cm}^{-1}$  is sensitive to the presence of oxygen vacancies in  $\text{In}_2\text{O}_3$ , and the ratio of the peak areas between 305 ( $I_1$ ) and 360  $\text{cm}^{-1}$  ( $I_2$ ) is usually adopted to quantify the relative content change in oxygen vacancies.<sup>63,64</sup> As shown in Figure 5D, the ratio for  $\text{In}_2\text{O}_3$  varies significantly by switching from  $\text{CO}_2$  to  $\text{C}_3\text{H}_8/\text{CO}_2$ , and it appears to have more oxygen vacancies under reaction conditions than that in  $\text{CO}_2$  alone. Recently, Hess et al. reported the oxygen and vacancy diffusion on  $\text{In}_2\text{O}_3$  at elevated temperatures, in which the oxygen atoms diffuse to the surface for oxidation, creating oxygen defects in the bulk.<sup>62</sup> Combined with this self-diffusion of oxygen, the surface of  $\text{In}_2\text{O}_3$  alone is likely partially reduced due to the presence of the reducing agent  $\text{C}_3\text{H}_8$ , while  $\text{CO}_2$  can reoxidize the catalyst. In contrast, the intensity ratio of 3.4V/In is relatively stable in  $\text{CO}_2$  and  $\text{C}_3\text{H}_8/\text{CO}_2$  (Figure 5D), signifying the role of  $\text{VO}_x$  in inhibiting the deep reduction of  $\text{In}_2\text{O}_3$  under  $\text{CO}_2$ -ODHP reaction conditions, as well as in impeding the contact between  $\text{CO}_2$  and surface vacancies for PDR.

DFT calculations were performed to study the effect of  $\text{VO}_x$  on the formation of vacancies on  $\text{In}_2\text{O}_3$ , and a model  $\text{V}_2\text{O}_5$  dimer on  $\text{In}_2\text{O}_3$  (110) was tested. As shown in Figure S16, the  $\text{V}_2\text{O}_5$  dimer increases the oxygen vacancy formation energies to a certain extent for most lattice oxygen, such as the sites which are directly underneath  $\text{VO}_x$  (Table S6). This simple model corroborates the role of  $\text{VO}_x$  in inhibiting the deep reduction of  $\text{In}_2\text{O}_3$ . The Raman peaks of  $\text{In}-\text{O}-\text{V}$  structure and  $\text{V}=\text{O}$  in polyvanadate show an evident decrease in intensity under reaction conditions (Figure 5C). By referring the peak area of  $\text{VO}_x$  ( $I_3$ ) to that of  $I_1$  (305  $\text{cm}^{-1}$ ) (Figure 5D), quantification analysis reveals that the normalized area of  $\text{VO}_x$  decreases in the  $\text{C}_3\text{H}_8/\text{CO}_2$  environment and recovers in the followed  $\text{CO}_2$  treatment. This signifies a potential redox cycle of  $\text{VO}_x$  under  $\text{CO}_2$ -ODHP reaction conditions via a MvK mechanism.<sup>27</sup>

**3.3.2. Redox Behaviors.** To gain insights into the redox characters and oxidation states, in situ NAP-XPS was

performed on 3.4V/In and  $\text{In}_2\text{O}_3$  under conditions similar to the reaction. Figure 6A,B presents the respective In 3d XPS spectra of  $\text{In}_2\text{O}_3$  and 3.4V/In under consecutive treatments in  $\text{O}_2$ ,  $\text{CO}_2$ ,  $\text{C}_3\text{H}_8/\text{CO}_2$ , and  $\text{CO}_2$  again after the reaction at 500 °C. Based on  $\text{H}_2$ -TPR and Raman results and catalytic performance, we expected to observe different reduction behaviors of surface indium oxide species between  $\text{In}_2\text{O}_3$  and 3.4V/In, wherein 3.4V/In should be more resistant to reduction. However, the metallic  $\text{In}^0$  species are absent for both catalysts and nor can be found in In MNN Auger spectra (Figure S17). A possible explanation is the diffusion of oxygen vacancies between the surface and the bulk of  $\text{In}_2\text{O}_3$ , which can maintain the surface In species under oxidized conditions.<sup>62</sup> The bulk reduction via such an oxygen migration is discernible from the in situ Raman results (Figure 5). Of note, volatilization of the metallic  $\text{In}^0$  phase is possible at high temperatures. TGA analysis indicates that the weight loss (due to the potential volatilization of  $\text{In}^0$ ) of  $\text{In}_2\text{O}_3$  and 3.4V/In in  $\text{N}_2$  is limited after three-cycle measurements (Figure S18).

Figure 6C shows the XP spectra of 3.4V/In in the region of V 2p<sub>3/2</sub> under similar consecutive treatments. The position of the maximal intensity barely changes, but the shape of the V 2p signal becomes less symmetric when  $\text{C}_3\text{H}_8$  is present. This suggests the evolution of  $\text{V}^{4+}$  species under reaction conditions, especially in  $\text{C}_3\text{H}_8$  alone. Besides, the normalized area of the V 2p<sub>3/2</sub> region decreases after the exposure to  $\text{C}_3\text{H}_8$  in the gas flow, implying the depletion of possibly reduced V into the bulk under reducing conditions. For the last three treatments, deconvolution analysis shows that the composition of  $\text{V}^{4+}$  decreases in the following order:  $\text{C}_3\text{H}_8 > \text{C}_3\text{H}_8/\text{CO}_2 > \text{CO}_2$  (Table S7). Clearly, the joint presence of  $\text{V}^{4+}$  and  $\text{V}^{5+}$  under reaction conditions demonstrates the presence of a  $\text{VO}_x$  redox cycle under reaction conditions, in line with the Raman results. This also corroborates the contribution of  $\text{VO}_x$  to the overall activity performance via a MvK mechanism.<sup>1,27</sup>

To provide more information in the redox cycle of  $\text{VO}_x$  and coordination environment of the catalysts, in situ XAS experiments were performed. Detailed data processing and analysis are elaborated in the Supporting Information (Figures S19–S25 and Tables S8–S16). Figure 7A shows the V K edge XANES spectra of 3.4V/In as synthesized and after four sequential treatments including 2.5%  $\text{CO}_2$ , 2.5%  $\text{CO}_2$  + 2.5%  $\text{C}_3\text{H}_8$ , 2.5%  $\text{C}_3\text{H}_8$  (post reaction), and 2.5%  $\text{CO}_2$  (post reaction), with each treatment carried out at 500 °C for 30 min. For comparison, the XANES spectra of 3.4V/In under

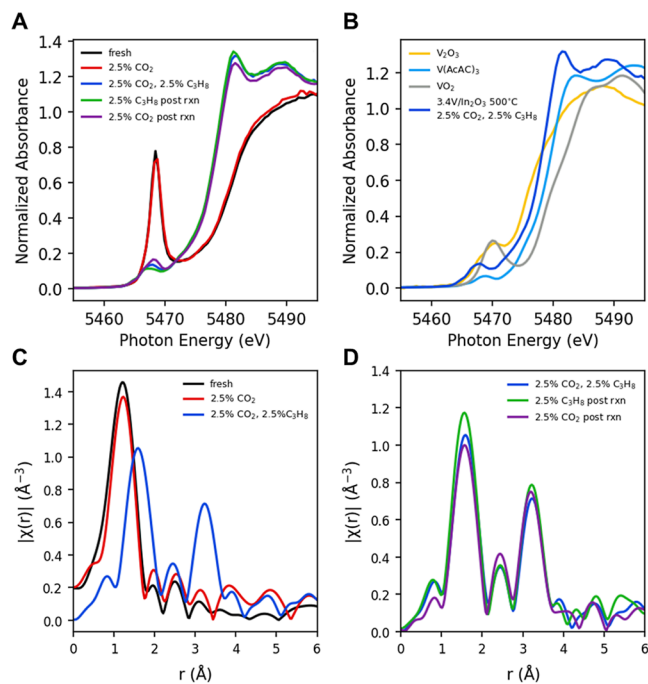


**Figure 7.** Vanadium K edge XANES spectra of 3.4V/In as synthesized and after in situ treatments (A), as well as the comparison between V K edge XANES spectrum of 3.4V/In after treatment in 2.5% CO<sub>2</sub> + 2.5% C<sub>3</sub>H<sub>8</sub> (balance He) and V references V<sub>2</sub>O<sub>3</sub>, V(AcAc)<sub>3</sub>, and VO<sub>2</sub> (B). (C) R space V K edge EXAFS spectra of fresh 3.4V/In and the same catalyst after sequential treatment in 2.5% CO<sub>2</sub> and 2.5% CO<sub>2</sub> + 2.5% C<sub>3</sub>H<sub>8</sub>, as well as those after sequential treatments in 2.5% C<sub>3</sub>H<sub>8</sub> and 2.5% CO<sub>2</sub> after the reaction in 2.5% CO<sub>2</sub> + 2.5% C<sub>3</sub>H<sub>8</sub> (D). Treatment conditions are detailed in Table S8.

C<sub>3</sub>H<sub>8</sub>/CO<sub>2</sub> is plotted with reference materials V<sub>2</sub>O<sub>3</sub>, VO<sub>2</sub>, and V(AcAc)<sub>3</sub> in Figure 7B. The pre-edge peak of 3.4V/In after the treatment in C<sub>3</sub>H<sub>8</sub>/CO<sub>2</sub> is at a lower energy than V(AcAc)<sub>3</sub> and an intensity intermediate between V<sub>2</sub>O<sub>3</sub> and V(AcAc)<sub>3</sub>, implying that vanadium has a local environment distinct from the octahedral or distorted octahedral symmetry of V(AcAc)<sub>3</sub> or V<sub>2</sub>O<sub>3</sub>. The edge position that lies between the two V<sup>3+</sup> references suggests that V is in the 3+ oxidation state. This is consistent with the XPS results, in which V<sup>3+</sup> is missing from the surface region, and some of the V is depleted from the surface region under C<sub>3</sub>H<sub>8</sub>. The XANES of samples treated post reaction sequentially in C<sub>3</sub>H<sub>8</sub>-post and then in CO<sub>2</sub>-post show subtle variation in pre-edge shape and edge energy compared to the one treated in C<sub>3</sub>H<sub>8</sub>/CO<sub>2</sub> (Figure 7A). This could be caused by partial redox or due to adsorbates on surface vanadium sites.

**Table 2. Structural Parameters of V–O and V–M Coordination Shells for 3.4V/In Catalysts Treated under Different Conditions**

| treatment                                      | V–O       |               | V–(C/O) <sup>a</sup> |               | V–V       |               | V–In      |               |
|--|-----------|---------------|----------------------|---------------|-----------|---------------|-----------|---------------|
|  | CN        | R (Å)         | CN                   | R (Å)         | CN        | R (Å)         | CN        | R (Å)         |
| Fresh  | 5.3 ± 1.6 | 1.67 ± 0.02   |                      |               |           |               |           |               |
| CO <sub>2</sub>                                | 4.2 ± 1.3 | 1.69 ± 0.02   |                      |               |           |               |           |               |
| C <sub>3</sub> H <sub>8</sub> /CO <sub>2</sub> | 3.5 ± 0.4 | 2.066 ± 0.006 | 0.3 ± 0.2            | 1.672 ± 0.006 | 1.4 ± 0.6 | 3.265 ± 0.009 | 6.0 ± 1.0 | 3.365 ± 0.009 |
| C <sub>3</sub> H <sub>8</sub> -post            | 3.5 ± 0.4 | 2.063 ± 0.006 | 0.5 ± 0.2            | 1.629 ± 0.005 | 0.8 ± 0.5 | 3.262 ± 0.009 | 5.1 ± 0.9 | 3.363 ± 0.009 |
| CO <sub>2</sub> -post                          | 2.9 ± 0.3 | 2.057 ± 0.005 | 0.2 ± 0.1            | 1.591 ± 0.005 | 1.3 ± 0.5 | 3.252 ± 0.008 | 5.5 ± 0.8 | 3.353 ± 0.008 |

<sup>a</sup>The second light scatterer in the first shell is V–C for C<sub>3</sub>H<sub>8</sub>/CO<sub>2</sub> and C<sub>3</sub>H<sub>8</sub>-post and is V–O for CO<sub>2</sub>-post.

Figure 7C,D shows the V K edge R space EXAFS of 3.4V/In after the same sequential treatments, along with the structural parameters in Table 2. The fresh and CO<sub>2</sub>-treated catalysts have similar spectra, with a single large peak centered at 1.2 Å (phase uncorrected distance) due to V–O scattering. After the treatment in CO<sub>2</sub>, V–O coordination number drops to 4.2, which is likely due to the dehydration. The short V–O bond distance (1.65 Å) and V–O coordination number (4–5) are consistent with V in the 5+ oxidation state. No distinct structure is observed past the first shell which reflects the configurational complexity of surface vanadium sites. In contrast, after the treatment in C<sub>3</sub>H<sub>8</sub>/CO<sub>2</sub>, strong second and third shell scatterings are seen. This implies a more crystalline local structure around vanadium after treatment. To model the structure after C<sub>3</sub>H<sub>8</sub>/CO<sub>2</sub> treatment, it was necessary to include both a V–O bond and a V–C bond to properly fit the first shell. The extended structure was modeled using V–V and V–In scattering paths within an In–V mixed oxide. The long V–O bond distance (2.066 Å) is consistent with a more reduced vanadium and in agreement with the reduced edge energy seen in the XANES. The appearance of a more ordered V environment after C<sub>3</sub>H<sub>8</sub>/CO<sub>2</sub> treatment may explain the difference in the oxidation state seen in XAS versus by XPS measurement. While XPS only measures V species in the near surface region, XAS measures all V present in the sample. The reduction to V<sup>3+</sup> may allow vanadium to diffuse into the In<sub>2</sub>O<sub>3</sub> lattice rapidly, which would explain the intensity loss in XPS after reducing treatment and the appearance of an ordered V environment in XAS.

After the treatment in the C<sub>3</sub>H<sub>8</sub>-post reaction (Figure 7D), the V–O coordination number remains unchanged, while the V–V and V–In coordination numbers drop by 0.6 and 0.9, respectively. The V–C coordination number increases from 0.3 to 0.5. A subsequent treatment in CO<sub>2</sub>-post reaction increases the V–M (V or In) coordination numbers close to the values seen after the C<sub>3</sub>H<sub>8</sub>/CO<sub>2</sub> treatment. In the first shell, the CO<sub>2</sub> post reaction treatment causes the V–O coordination number to change from 3.5 to 2.9. Additionally, all V–C coordination is lost, and instead a short V–O bond is observed at 1.591 Å, indicative of the oxidation of V to higher oxidation states.

Taken together, these changes in coordination numbers show that under reaction conditions (C<sub>3</sub>H<sub>8</sub>/CO<sub>2</sub>), vanadium reduces and forms a mixed oxide with In<sub>2</sub>O<sub>3</sub>. A fraction of surface vanadium sites has bonded with a carbon-containing species, likely derived from propane under conditions of both C<sub>3</sub>H<sub>8</sub>/CO<sub>2</sub> and C<sub>3</sub>H<sub>8</sub> alone. When treated in C<sub>3</sub>H<sub>8</sub> alone, this surface coverage of carbon-containing species increases, and the V–M coordination number decreases. Likely, the reduction, occurring in the subsurface, results in the loss of

oxygen and breaking of In–O–V (as evidenced by a smaller V–O coordination number), followed by the self-diffusion of bulk oxygen to oxidize the surface.<sup>62</sup> This agrees with the observations from Raman results, in which the reduction and reoxidation of  $\text{In}_2\text{O}_3$  are evidenced in the presence of  $\text{C}_3\text{H}_8$  and  $\text{CO}_2$ , respectively (Figure 5). Treating in  $\text{CO}_2$  removes the carbon-containing species bonded to V and regenerates the V–O bond. These results are consistent with vanadium sites acting as binding sites for propane adsorption and dehydrogenation and with  $\text{CO}_2$  acting as a soft oxidant facilitating its removal.

#### 4. DISCUSSION

Raman and UV-vis DRS results reveal the presence of the In–O–V structure and dispersed polyvanadates for 3.4V/In with the optimal composition for the  $\text{CO}_2$ -ODHP performance. In situ Raman, NAP-XPS, and XAS spectra provide strong evidence of the redox cycle of  $\text{VO}_x$  under reaction conditions, wherein  $\text{CO}_2$  plays a role in reoxidizing  $\text{V}^{3+}/\text{V}^{4+}$  to  $\text{V}^{5+}$ . It is critical to link these observations with the acid–base and redox properties of  $\text{VO}_x/\text{In}_2\text{O}_3$  catalysts, as well as to advance the understanding of their correlations with the well-retained high  $\text{C}_3\text{H}_6$  selectivity and improved stability.

$\text{In}_2\text{O}_3$  is a known catalyst candidate for ODHP reactions; however, its reaction mechanism is elusive.<sup>11,33</sup> Our in situ Raman results demonstrate the reduction and reoxidation of  $\text{In}_2\text{O}_3$  under  $\text{C}_3\text{H}_8/\text{CO}_2$  and  $\text{CO}_2$  conditions, respectively (Figure 5). Although Raman probes the bulk, the redox has to start from the surface and then dynamically propagates into the bulk. Besides, the identified reducible  $\text{In}_2\text{O}_3$  species that have intimate interactions with  $\text{VO}_x$  species from  $\text{H}_2$ -TPR profiles (160–230 °C from Figure 4A) are likely those redox-active  $\text{InO}_x$  species. Thus, the redox property of  $\text{InO}_x$  might play a role in  $\text{CO}_2$ -ODHP, similar to MvK on  $\text{VO}_x$ .<sup>1</sup> However, in situ NAP-XPS and AES results present a stable oxidation state of In species on the surface (Figure 6). Likely, the redox cycle happens too fast to be captured, or volatilization of metallic In may occur, both of which are responsible for the missing metallic In phase from spectra. As a result, even if the redox cycle of  $\text{InO}_x$  indeed presents, it is limited based on our observations. In other words, both heterolytic dissociation and MvK are possible for  $\text{In}_2\text{O}_3$  for  $\text{CO}_2$ -ODHP. This is the place where more effort is needed in the future.

Our NAP-XPS results indicate that the surface In species stay at a stable oxidation state in the case for  $\text{In}_2\text{O}_3$  during reactions (Figure 6). Thus, a similar heterolytic dissociation mechanism might be applicable to  $\text{In}_2\text{O}_3$ . Based on  $\text{H}_2$ -TPR and Raman results, a deep reduction of  $\text{In}_2\text{O}_3$  occurs at higher temperatures (>500 °C, Figures 4 and S11), which results in decreased selectivity and deactivation. The first crucial role of surface vanadates and the bridging In–O–V structure is to help resist the deep reduction of  $\text{In}_2\text{O}_3$  under reaction conditions, therefore maintaining the selectivity and improving the stability for  $\text{CO}_2$ -ODHP.

$\text{In}_2\text{O}_3$  is a basic metal oxide that features  $\text{CO}_2$  adsorption on oxygen vacancies.<sup>35,49,63,65,66</sup> However, such a strong affinity toward  $\text{CO}_2$  may “poison” the surface to favor  $\text{CO}_2$  adsorption and activation for side reactions such as PDR. Most recently, by studying a series of Pd bimetallic catalysts for  $\text{CO}_2$ -assisted ethane dehydrogenation, Chen et al. showed that a metallic surface favors dry reforming, while an oxidic surface favors C–H scission in ethane.<sup>67</sup> Linked to our observations, it is suggested that the reduction of  $\text{In}_2\text{O}_3$  under reaction

conditions is another reason resulting in PDR and impairing the  $\text{C}_3\text{H}_8$  dehydrogenation on  $\text{In}_2\text{O}_3$ . The presence of vanadates neutralizes these basic sites and inhibits the deep reduction of  $\text{In}_2\text{O}_3$ , as evidenced by the chemisorption results (Figure 4 and Table 1). This further enables the suppression of PDR, resulting in an enhanced  $\text{C}_3\text{H}_6$  selectivity.

Studies of reaction paths in the current work shows that  $\text{CO}_2$ -ODHP proceeds more through a one-cycle mechanism. In specific,  $\text{CO}_2$  can form CO without undergoing a separate RWGS step. In this case,  $\text{CO}_2$  plays a role in reoxidizing the  $\text{VO}_x$  and potentially  $\text{InO}_x$  to close the redox cycles, releasing CO and  $\text{H}_2\text{O}$  as products. Noteworthily, the produced amount of CO is much less in  $\text{CO}_2$ -ODHP than that in PDR, which can be reflected from the retained higher  $\text{C}_3\text{H}_6$  selectivity over V/In catalysts than that over  $\text{In}_2\text{O}_3$ . Therefore, the second role of  $\text{VO}_x$  is to shift the role of  $\text{CO}_2$  from contributing to PDR on  $\text{In}_2\text{O}_3$  to completing the redox cycle for propane dehydrogenation as a soft oxidant. This is a promising way of utilizing the reagent molecules for a desired reaction pathway.

#### 5. CONCLUSIONS

In this work, we prepared a series of  $\text{VO}_x/\text{In}_2\text{O}_3$  with various surface V densities and compared the activity performance with  $\text{In}_2\text{O}_3$  alone for  $\text{CO}_2$ -ODHP. On  $\text{In}_2\text{O}_3$ , the  $\text{C}_3\text{H}_6$  selectivity decreases sharply with the increase in  $\text{C}_3\text{H}_8$  conversion and drops below 50% beyond 4%  $\text{C}_3\text{H}_8$  conversion, as well as poor stability. This can be ascribed to the strong basicity and reduced  $\text{In}_2\text{O}_3$  during ODHP that favor PDR to CO when the deep reduction occurs, especially at higher temperatures. In contrast, all  $\text{VO}_x$ -loaded catalysts not only present higher  $\text{C}_3\text{H}_6$  selectivity than  $\text{In}_2\text{O}_3$  under isoconventional conditions (higher than 60% at 4%  $\text{C}_3\text{H}_8$  conversion), but they also exhibit improved stability. The optimal surface V density is obtained at 3.4V nm<sup>-2</sup> for  $\text{CO}_2$ -ODHP. Detailed characterization results identify the bridging In–O–V structure and dispersed mono-/polyvanadate on  $\text{In}_2\text{O}_3$  at the  $\text{VO}_x$  loading below a monolayer coverage (between 3.4 and 4.6V/nm<sup>2</sup>). The presence of the In–O–V structure and dispersed  $\text{VO}_x$  species can help resist  $\text{In}_2\text{O}_3$  reduction and suppress PDR, resulting in better selectivity and stability. Also,  $\text{VO}_x$  itself contributes to the overall catalytic performance through the redox cycle by using  $\text{CO}_2$  as a soft oxidant. These findings provide insights into designing selective, robust catalysts for the  $\text{CO}_2$ -ODHP reaction by manipulating the interplays between the redox property and acid–base interaction in catalysts based on mixed oxides.

#### ■ ASSOCIATED CONTENT

##### Supporting Information

The Supporting Information is available free of charge at <https://pubs.acs.org/doi/10.1021/acscatal.2c02099>.

Detailed ICP results; additional results of activity tests, kinetic studies, and MS results; activity data of RWGS; coke analysis via  $\text{O}_2$ -TPO;  $\text{H}_2$ -TPR profiles,  $\text{NH}_3$ -DRIFTS, and  $\text{CO}_2$ -DRIFTS spectra; in situ Raman spectra collected under pretreatment and reaction conditions; DFT methods and model structures; in situ NAP-XPS spectra and quantification results; TGA profiles after cycles; and in situ XAS spectra and data analysis (PDF)

## AUTHOR INFORMATION

### Corresponding Authors

**Israel E. Wachs** — Department of Chemical & Biomolecular Engineering, Lehigh University, Bethlehem, Pennsylvania 18015, United States;  [orcid.org/0000-0001-5282-128X](https://orcid.org/0000-0001-5282-128X); Email: [iw0@lehigh.edu](mailto:iw0@lehigh.edu)

**Zili Wu** — Chemical Sciences Division, Oak Ridge National Laboratory, Oak Ridge, Tennessee 37831, United States; Center for Nanophase Materials Sciences, Oak Ridge National Laboratory, Oak Ridge, Tennessee 37831, United States;  [orcid.org/0000-0002-4468-3240](https://orcid.org/0000-0002-4468-3240); Email: [wuz1@ornl.gov](mailto:wuz1@ornl.gov)

### Authors

**Xiao Jiang** — Chemical Sciences Division, Oak Ridge National Laboratory, Oak Ridge, Tennessee 37831, United States;  [orcid.org/0000-0002-4902-1828](https://orcid.org/0000-0002-4902-1828)

**Bar Mosevitzky Lis** — Department of Chemical & Biomolecular Engineering, Lehigh University, Bethlehem, Pennsylvania 18015, United States;  [orcid.org/0001-5793-5358](https://orcid.org/0001-5793-5358)

**Stephen C. Purdy** — Neutron Scattering Division, Oak Ridge National Laboratory, Oak Ridge, Tennessee 37830, United States;  [orcid.org/0000-0002-9870-1029](https://orcid.org/0000-0002-9870-1029)

**Sreya Paladugu** — Department of Materials Science and Engineering, University of Tennessee, Knoxville, Tennessee 37996, United States

**Victor Fung** — Center for Nanophase Materials Sciences, Oak Ridge National Laboratory, Oak Ridge, Tennessee 37831, United States;  [orcid.org/0000-0002-3347-6983](https://orcid.org/0000-0002-3347-6983)

**Wenying Quan** — School of Chemical & Biomolecular Engineering, Georgia Institute of Technology, Atlanta, Georgia 30332, United States

**Zhenghong Bao** — Chemical Sciences Division, Oak Ridge National Laboratory, Oak Ridge, Tennessee 37831, United States;  [orcid.org/0000-0002-4615-9741](https://orcid.org/0000-0002-4615-9741)

**Weiwei Yang** — Chemical Sciences Division, Oak Ridge National Laboratory, Oak Ridge, Tennessee 37831, United States

**Yang He** — Chemical Sciences Division, Oak Ridge National Laboratory, Oak Ridge, Tennessee 37831, United States

**Bobby G. Sumpter** — Center for Nanophase Materials Sciences, Oak Ridge National Laboratory, Oak Ridge, Tennessee 37831, United States;  [orcid.org/0000-0001-6341-0355](https://orcid.org/0000-0001-6341-0355)

**Katharine Page** — Neutron Scattering Division, Oak Ridge National Laboratory, Oak Ridge, Tennessee 37830, United States; Department of Materials Science and Engineering, University of Tennessee, Knoxville, Tennessee 37996, United States;  [orcid.org/0000-0002-9071-3383](https://orcid.org/0000-0002-9071-3383)

Complete contact information is available at:

<https://pubs.acs.org/10.1021/acscatal.2c02099>

### Notes

The authors declare no competing financial interest.

## ACKNOWLEDGMENTS

This work was supported as part of the Center for Understanding and Control of Acid Gas-Induced Evolution of Materials for Energy (UNCAGE ME), an Energy Frontier Research Center funded by the U.S. Department of Energy, Office of Science, Basic Energy Sciences at the under award #

DE-SC0012577. Part of the work including the synthesis, activity test, DFT calculations, and characterizations (chemisorption, DRIFTS, and in situ Raman Spectroscopy) was carried out at the Center for Nanophase Materials Sciences, which is a DOE Office of Science User Facility. MRCAT operations are supported by the Department of Energy and the MRCAT member institutions. This research used resources of the Advanced Photon Source, a U.S. Department of Energy (DOE) Office of Science User Facility operated for the DOE Office of Science by Argonne National Laboratory under Contract no. DE-AC02-06CH11357. In situ NAP-XPS and Part of the in situ Raman spectroscopy were performed at the Operando Molecular Spectroscopy and Catalysis Research Laboratory at Lehigh University.

## REFERENCES

- (1) Carrero, C. A.; Schloegl, R.; Wachs, I. E.; Schomaecker, R. Critical Literature Review of the Kinetics for the Oxidative Dehydrogenation of Propane over Well-Defined Supported Vanadium Oxide Catalysts. *ACS Catal.* **2014**, *4*, 3357–3380.
- (2) Sattler, J. J.; Ruiz-Martinez, J.; Santillan-Jimenez, E.; Weckhuysen, B. M. Catalytic Dehydrogenation of Light Alkanes on Metals and Metal Oxides. *Chem. Rev.* **2014**, *114*, 10613–10653.
- (3) Zhao, G. L.; Teng, J. W.; Xie, Z. K.; Yang, W. M.; Chen, Q. L.; Tang, Y. Catalytic Cracking Reactions of C<sub>4</sub>-Olefin over Zeolites H-ZSM-5, H-Mordenite and H-SAPO-34. *Stud. Surf. Sci. Catal.* **2007**, *170*, 1307–1312.
- (4) Zhao, Z. J.; Chiu, C. C.; Gong, J. Molecular Understandings on the Activation of Light Hydrocarbons over Heterogeneous Catalysts. *Chem. Sci.* **2015**, *6*, 4403–4425.
- (5) Hu, Z.-P.; Yang, D.; Wang, Z.; Yuan, Z.-Y. State-of-the-Art Catalysts for Direct Dehydrogenation of Propane to Propylene. *Chin. J. Catal.* **2019**, *40*, 1233–1254.
- (6) Larsson, M.; Hultén, M.; Blekkan, E. A.; Andersson, B. The Effect of Reaction Conditions and Time on Stream on the Coke Formed during Propane Dehydrogenation. *J. Catal.* **1996**, *164*, 44–53.
- (7) Galvita, V.; Siddiqi, G.; Sun, P.; Bell, A. T. Ethane Dehydrogenation on Pt/Mg(Al)O and PtSn/Mg(Al)O Catalysts. *J. Catal.* **2010**, *271*, 209–219.
- (8) Siddiqi, G.; Sun, P.; Galvita, V.; Bell, A. T. Catalyst Performance of Novel Pt/Mg(Ga)(Al)O Catalysts for Alkane Dehydrogenation. *J. Catal.* **2010**, *274*, 200–206.
- (9) Saerens, S.; Sabbe, M. K.; Galvita, V. V.; Redekop, E. A.; Reyniers, M.-F.; Marin, G. B. The Positive Role of Hydrogen on the Dehydrogenation of Propane on Pt(111). *ACS Catal.* **2017**, *7*, 7495–7508.
- (10) Purdy, S. C.; Seemakurthi, R. R.; Mitchell, G. M.; Davidson, M.; Lauderback, B. A.; Deshpande, S.; Wu, Z.; Wegener, E. C.; Greeley, J.; Miller, J. T. Structural Trends in the Dehydrogenation Selectivity of Palladium Alloys. *Chem. Sci.* **2020**, *11*, 5066–5081.
- (11) Atanga, M. A.; Rezaei, F.; Jawad, A.; Fitch, M.; Rownaghi, A. A. Oxidative Dehydrogenation of Propane to Propylene with Carbon Dioxide. *Appl. Catal., B* **2018**, *220*, 429–445.
- (12) Grant, J. T.; Carrero, C. A.; Goeltl, F.; Venegas, J.; Mueller, P.; Burt, S. P.; Specht, S. E.; McDermott, W. P.; Chieregato, A.; Hermans, I. Selective Oxidation Dehydrogenation of Propane to Propene Using Boron Nitride Catalysts. *Science* **2016**, *354*, 1570–1573.
- (13) Zhou, H.; Yi, X.; Hui, Y.; Wang, L.; Chen, W.; Qin, Y.; Wang, M.; Ma, J.; Chu, X.; Wang, Y.; Hong, X.; Chen, Z.; Meng, X.; Wang, H.; Zhu, Q.; Song, L.; Zheng, A.; Xiao, F.-S. Isolated Boron in Zeolite for Oxidative Dehydrogenation of Propane. *Science* **2021**, *372*, 76–80.
- (14) Tian, J.; Tan, J.; Xu, M.; Zhang, Z.; Wan, S.; Wang, S.; Lin, J.; Wang, Y. Propane Oxidative Dehydrogenation over Highly Selective Hexagonal Boron Nitride Catalysts: The Role of Oxidative Coupling of Methyl. *Sci. Adv.* **2019**, *5*, No. eaav8063.

- (15) Altvater, N. R.; Dorn, R. W.; Cendejas, M. C.; McDermott, W. P.; Thomas, B.; Rossini, A. J.; Hermans, I. B-MWW Zeolite: The Case Against Single-Site Catalysis. *Angew. Chem., Int. Ed.* **2020**, *59*, 6546–6550.
- (16) Venegas, J. M.; Zhang, Z.; Agbi, T. O.; McDermott, W. P.; Alexandrova, A.; Hermans, I. Why Boron Nitride is such a Selective Catalyst for the Oxidative Dehydrogenation of Propane. *Angew. Chem., Int. Ed.* **2020**, *59*, 16527–16535.
- (17) Mark, L. O.; Dorn, R. W.; McDermott, W. P.; Agbi, T. O.; Altavater, N. R.; Jansen, J.; Lebrón-Rodríguez, E. A.; Cendejas, M. C.; Rossini, A. J.; Hermans, I. Highly Selective Carbon-Supported Boron for Oxidative Dehydrogenation of Propane. *ChemCatChem* **2021**, *13*, 3611–3618.
- (18) Yan, H.; Alayoglu, S.; Wu, W.; Zhang, Y.; Weitz, E.; Stair, P. C.; Notestein, J. M. Identifying Boron Active Sites for the Oxidative Dehydrogenation of Propane. *ACS Catal.* **2021**, *11*, 9370–9376.
- (19) Cavani, F.; Ballarini, N.; Cericola, A. Oxidative Dehydrogenation of Ethane and Propane: How Far from Commercial Implementation? *Catal. Today* **2007**, *127*, 113–131.
- (20) Burri, A.; Hasib, M. A.; Mo, Y.-H.; Reddy, B. M.; Park, S.-E. An Efficient Cr-TUD-1 Catalyst for Oxidative Dehydrogenation of Propane to Propylene with CO<sub>2</sub> as Soft Oxidant. *Catal. Lett.* **2017**, *148*, 576–585.
- (21) Zhang, Y.; Cho, Y.; Yamaguchi, A.; Peng, X.; Miyauchi, M.; Abe, H.; Fujita, T. CO<sub>2</sub> Oxidative Coupling of Methane Using An Earth-Abundant CaO-based Catalyst. *Sci. Rep.* **2019**, *9*, 15454.
- (22) Zhang, L.; Wu, Z.; Nelson, N. C.; Sadow, A. D.; Slowing, I. I.; Overbury, S. H. Role of CO<sub>2</sub> As A Soft Oxidant for Dehydrogenation of Ethylbenzene to Styrene over A High-Surface-Area Ceria Catalyst. *ACS Catal.* **2015**, *5*, 6426–6435.
- (23) Gomez, E.; Kattel, S.; Yan, B.; Yao, S.; Liu, P.; Chen, J. G. Combining CO<sub>2</sub> Reduction with Propane Oxidative Dehydrogenation over Bimetallic Catalysts. *Nat. Commun.* **2018**, *9*, 1398.
- (24) Otroshchenko, T.; Jiang, G.; Kondratenko, V. A.; Rodemerck, U.; Kondratenko, E. V. Current Status and Perspectives in Oxidative, Non-Oxidative and CO<sub>2</sub>-Mediated Dehydrogenation of Propane and Isobutane over Metal Oxide Catalysts. *Chem. Soc. Rev.* **2021**, *50*, 473–527.
- (25) Chen, M.; Wu, J.-L.; Liu, Y.-M.; Cao, Y.; Guo, L.; He, H.-Y.; Fan, K.-N. Study in Support Effect of In<sub>2</sub>O<sub>3</sub>/MO<sub>x</sub> (M=Al, Si, Zr) Catalysts for Dehydrogenation of Propane in the Presence of CO<sub>2</sub>. *Appl. Catal., A* **2011**, *407*, 20–28.
- (26) Shimada, H.; Akazawa, T.; Ikenaga, N.-o.; Suzuki, T. Dehydrogenation of Isobutane to Isobutene with Iron-Loaded Activated Carbon Catalyst. *Appl. Catal., A* **1998**, *168*, 243–250.
- (27) Jiang, X.; Sharma, L.; Fung, V.; Park, S. J.; Jones, C. W.; Sumpter, B. G.; Baltrusaitis, J.; Wu, Z. Oxidative Dehydrogenation of Propane to Propylene with Soft Oxidants via Heterogeneous Catalysis. *ACS Catal.* **2021**, *11*, 2182–2234.
- (28) Xu, B.; Zheng, B.; Hua, W.; Yue, Y.; Gao, Z. Support Effect in Dehydrogenation of Propane in the Presence of CO<sub>2</sub> over Supported Gallium Oxide Catalysts. *J. Catal.* **2006**, *239*, 470–477.
- (29) Ascoop, I.; Galvita, V. V.; Alexopoulos, K.; Reyniers, M.-F.; Van Der Voort, P.; Bliznuk, V.; Marin, G. B. The Role of CO<sub>2</sub> in the Dehydrogenation of Propane over WO<sub>x</sub>–VO<sub>x</sub>/SiO<sub>2</sub>. *J. Catal.* **2016**, *335*, 1–10.
- (30) Wang, Z. Y.; He, Z. H.; Li, L. Y.; Yang, S. Y.; He, M. X.; Sun, Y. C.; Wang, K.; Chen, J. G.; Liu, Z. T. Research Progress of CO<sub>2</sub> Oxidative Dehydrogenation of Propane to Propylene over Cr-Free Metal Catalysts. *Rare Met.* **2022**, *41*, 2129–2152.
- (31) Chen, M.; Xu, J.; Liu, Y.-M.; Cao, Y.; He, H.-Y.; Zhuang, J.-H.; Fan, K.-N. Enhanced Activity of Spinel-type Ga<sub>2</sub>O<sub>3</sub>–Al<sub>2</sub>O<sub>3</sub> Mixed Oxide for the Dehydrogenation of Propane in the Presence of CO<sub>2</sub>. *Catal. Lett.* **2008**, *124*, 369–375.
- (32) Chen, M.; Xu, J.; Su, F.; Liu, Y.; Cao, Y.; He, H.; Fan, K. Dehydrogenation of Propane over Spinel-Type Gallia–Alumina Solid Solution Catalysts. *J. Catal.* **2008**, *256*, 293–300.
- (33) Chen, M.; Xu, J.; Cao, Y.; He, H.-Y.; Fan, K.-N.; Zhuang, J.-H. Dehydrogenation of Propane over In<sub>2</sub>O<sub>3</sub>–Al<sub>2</sub>O<sub>3</sub> Mixed Oxide in the Presence of Carbon Dioxide. *J. Catal.* **2010**, *272*, 101–108.
- (34) Chen, M.; Xu, J.; Liu, Y.-M.; Cao, Y.; He, H.-Y.; Zhuang, J.-H. Supported Indium Oxide as Novel Efficient Catalysts for Dehydrogenation of Propane with Carbon Dioxide. *Appl. Catal., A* **2010**, *377*, 35–41.
- (35) Martin, O.; Martín, A. J.; Mondelli, C.; Mitchell, S.; Segawa, T. F.; Hauert, R.; Drouilly, C.; Curulla-Ferré, D.; Pérez-Ramírez, J. Indium Oxide as A Superior Catalyst for Methanol Synthesis by CO<sub>2</sub> Hydrogenation. *Angew. Chem., Int. Ed.* **2016**, *55*, 6261–6265.
- (36) Frei, M. S.; Capdevila-Cortada, M.; García-Muelas, R.; Mondelli, C.; López, N.; Stewart, J. A.; Curulla Ferré, D.; Pérez-Ramírez, J. Mechanism and Microkinetics of Methanol Synthesis via CO<sub>2</sub> Hydrogenation on Indium Oxide. *J. Catal.* **2018**, *361*, 313–321.
- (37) Frei, M. S.; Mondelli, C.; García-Muelas, R.; Kley, K. S.; Puértolas, B.; López, N.; Safonova, O. V.; Stewart, J. A.; Curulla Ferré, D.; Pérez-Ramírez, J. Atomic-Scale Engineering of Indium Oxide Promotion by Palladium for Methanol Production via CO<sub>2</sub> Hydrogenation. *Nat. Commun.* **2019**, *10*, 3377.
- (38) Gao, P.; Li, S.; Bu, X.; Dang, S.; Liu, Z.; Wang, H.; Zhong, L.; Qiu, M.; Yang, C.; Cai, J.; Wei, W.; Sun, Y. Direct Conversion of CO<sub>2</sub> into Liquid Fuels with High Selectivity over A Bifunctional Catalyst. *Nat. Chem.* **2017**, *9*, 1019–1024.
- (39) Zheng, B.; Hua, W.; Yue, Y.; Gao, Z. Dehydrogenation of Propane to Propene over Different Polymorphs of Gallium Oxide. *J. Catal.* **2005**, *232*, 143–151.
- (40) Liu, G.; Zhao, Z.-J.; Wu, T.; Zeng, L.; Gong, J. Nature of the Active Sites of VO<sub>x</sub>/Al<sub>2</sub>O<sub>3</sub> Catalysts for Propane Dehydrogenation. *ACS Catal.* **2016**, *6*, 5207–5214.
- (41) Detweiler, Z. M.; Wulfberg, S. M.; Frith, M. G.; Bocarsly, A. B.; Bernasek, S. L. The Oxidation and Surface Speciation of Indium and Indium Oxides Exposed to Atmospheric Oxidants. *Surf. Sci.* **2016**, *648*, 188–195.
- (42) Silversmit, G.; Depla, D.; Poelman, H.; Marin, G. B.; De Gryse, R. Determination of the V2p XPS Binding Energies for Different Vanadium Oxidation States (V<sup>5+</sup> to V<sup>0+</sup>). *J. Electron Spectrosc. Relat. Phenom.* **2004**, *135*, 167–175.
- (43) Schwarting, M.; Siol, S.; Talley, K.; Zakutayev, A.; Phillips, C. Automated Algorithms for Band Gap Analysis from Optical Absorption Spectra. *Mater. Discovery* **2017**, *10*, 43–52.
- (44) Kropf, A. J.; Katsoudas, J.; Chattopadhyay, S.; Shibata, T.; Lang, E. A.; Zyryanov, V. N.; Ravel, B.; McIvor, K.; Kemner, K. M.; Scheckel, K. G.; Bare, S. R.; Terry, J.; Kelly, S. D.; Bunker, B. A.; Segre, C. U. The New MIRCAT (Sector 10) Bending Magnet Beamline at the Advanced Photon Source. *AIP Conf. Proc.* **2010**, *1234*, 299–302.
- (45) Bolin, T. B.; Wu, T.; Schweitzer, N.; Lobo-Lapidus, R.; Kropf, A. J.; Wang, H.; Hu, Y.; Miller, J. T.; Heald, S. M. In situ Intermediate-Energy X-Ray Catalysis Research at the Advanced Photon Source Beamline 9-BM. *Catal. Today* **2013**, *205*, 141–147.
- (46) Park, P. W.; Ragle, C. S.; Boyer, C. L.; Balmer, M. L.; Engelhard, M.; McCready, D. In<sub>2</sub>O<sub>3</sub>/Al<sub>2</sub>O<sub>3</sub> Catalysts for NO<sub>x</sub> Reduction in Lean Condition. *J. Catal.* **2002**, *210*, 97–105.
- (47) Perdigonmelon, J.; Gervasini, A.; Auroux, A. Study of the Influence of the In<sub>2</sub>O<sub>3</sub> Loading on  $\gamma$ -Alumina for the Development of De-NO<sub>x</sub> Catalysts. *J. Catal.* **2005**, *234*, 421–430.
- (48) Xie, Y.; Luo, R.; Sun, G.; Chen, S.; Zhao, Z. J.; Mu, R.; Gong, J. Facilitating the Reduction of V-O Bonds on VO<sub>x</sub>/ZrO<sub>2</sub> Catalysts for Non-Oxidative Propane Dehydrogenation. *Chem. Sci.* **2020**, *11*, 3845–3851.
- (49) Rui, N.; Wang, Z.; Sun, K.; Ye, J.; Ge, Q.; Liu, C.-j. CO<sub>2</sub> Hydrogenation to Methanol over Pd/In<sub>2</sub>O<sub>3</sub>: Effects of Pd and Oxygen Vacancy. *Appl. Catal., B* **2017**, *218*, 488–497.
- (50) Bando, K. K.; Sayama, K.; Kusama, H.; Okabe, K.; Arakawa, H. In-situ FT-IR Study on CO<sub>2</sub> Hydrogenation over Cu Catalysts Supported on SiO<sub>2</sub>, Al<sub>2</sub>O<sub>3</sub> and TiO<sub>2</sub>. *Appl. Catal., A* **1997**, *165*, 391–409.

- (51) Collins, S. E.; Baltanas, M. A.; Bonivardi, A. L. An Infrared Study of the Intermediates of Methanol Synthesis from Carbon Dioxide over Pd/ $\beta$ -Ga<sub>2</sub>O<sub>3</sub>. *J. Catal.* **2004**, *226*, 410–421.
- (52) Lee, S. M.; Lee, Y. H.; Moon, D. H.; Ahn, J. Y.; Nguyen, D. D.; Chang, S. W.; Kim, S. S. Reaction Mechanism and Catalytic Impact of Ni/CeO<sub>2-x</sub> Catalyst for Low-Temperature CO<sub>2</sub> Methanation. *Ind. Eng. Chem. Res.* **2019**, *58*, 8656–8662.
- (53) Khader, M. M. Surface Acidity of V<sub>2</sub>O<sub>5</sub>/Al<sub>2</sub>O<sub>3</sub> Catalysts: IR and TPD Studies. *J. Mol. Catal. A: Chem.* **1995**, *104*, 87–94.
- (54) Burcham, L. J.; Deo, G.; Gao, X.; Wachs, I. E. In situ IR, Raman, and UV-Vis DRS Spectroscopy of Supported Vanadium Oxide Catalysts during Methanol Oxidation. *Top. Catal.* **2000**, *11/12*, 85–100.
- (55) Wu, Z.; Rondinone, A. J.; Ivanov, I. N.; Overbury, S. H. Structure of Vanadium Oxide Supported on Ceria by Multiwavelength Raman Spectroscopy. *J. Phys. Chem. C* **2011**, *115*, 25368–25378.
- (56) Haija, M. A.; Romanyshyn, Y.; Uhl, A.; Kuhlenbeck, H.; Freund, H. J. Carbon Dioxide Adsorption on V<sub>2</sub>O<sub>3</sub>(0001). *Top. Catal.* **2017**, *60*, 413–419.
- (57) Shvets, P.; Dikaya, O.; Maksimova, K.; Goikhman, A. A Review of Raman Spectroscopy of Vanadium Oxides. *J. Raman Spectrosc.* **2019**, *50*, 1226–1244.
- (58) Baran, E. J.; Escobar, M. E. The Vibrational Spectra of InVO<sub>4</sub> and TiVO<sub>4</sub>. *Spectrochim. Acta, Part A* **1985**, *41*, 415–417.
- (59) Weckhuysen, B. M.; Keller, D. E. Chemistry, Spectroscopy and the Role of Supported Vanadium Oxides in Heterogeneous Catalysis. *Catal. Today* **2003**, *78*, 25–46.
- (60) Xie, S.; Iglesia, E.; Bell, A. T. Effects of Hydration and Dehydration on the Structure of Silica-Supported Vanadia Species. *Langmuir* **2000**, *16*, 7162–7167.
- (61) Tian, H.; Ross, E. I.; Wachs, I. E. Quantitative Determination of the Speciation of Surface Vanadium Oxides and Their Catalytic Activity. *J. Phys. Chem. B* **2006**, *110*, 9593–9600.
- (62) Ziembka, M.; Schumacher, L.; Hess, C. Reduction Behavior of Cubic In<sub>2</sub>O<sub>3</sub> Nanoparticles by Combined Multiple In Situ Spectroscopy and DFT. *J. Phys. Chem. Lett.* **2021**, *12*, 3749–3754.
- (63) Shen, C.; Sun, K.; Zhang, Z.; Rui, N.; Jia, X.; Mei, D.; Liu, C.-j. Highly Active Ir/In<sub>2</sub>O<sub>3</sub> Catalysts for Selective Hydrogenation of CO<sub>2</sub> to Methanol: Experimental and Theoretical Studies. *ACS Catal.* **2021**, *11*, 4036–4046.
- (64) Gan, J.; Lu, X.; Wu, J.; Xie, S.; Zhai, T.; Yu, M.; Zhang, Z.; Mao, Y.; Wang, S. C.; Shen, Y.; Tong, Y. Oxygen Vacancies Promoting Photoelectrochemical Performance of In<sub>2</sub>O<sub>3</sub> Nanocubes. *Sci. Rep.* **2013**, *3*, 1021.
- (65) Ye, J.; Liu, C.; Mei, D.; Ge, Q. Active Oxygen Vacancy Site for Methanol Synthesis from CO<sub>2</sub> Hydrogenation on In<sub>2</sub>O<sub>3</sub>(110): A DFT Study. *ACS Catal.* **2013**, *3*, 1296–1306.
- (66) Ye, J.; Liu, C.; Ge, Q. DFT Study of CO<sub>2</sub> Adsorption and Hydrogenation on the In<sub>2</sub>O<sub>3</sub> Surface. *J. Phys. Chem. C* **2012**, *116*, 7817–7825.
- (67) Xie, Z.; Wang, X.; Chen, X.; Liu, P.; Chen, J. G. General Descriptors for CO<sub>2</sub>-Assisted Selective C-H/C-C Bond Scission in Ethane. *J. Am. Chem. Soc.* **2022**, *144*, 4186.

## □ Recommended by ACS

### Proving a Paradigm in Methanol Steam Reforming: Catalytically Highly Selective In<sub>x</sub>Pd<sub>y</sub>/In<sub>2</sub>O<sub>3</sub> Interfaces

Nicolas Köwitsch, Marc Armbrüster, et al.

DECEMBER 18, 2020

ACS CATALYSIS

READ ▶

### Preferential Oxidation of CO in Hydrogen at Nonmetal Active Sites with High Activity and Selectivity

Yongjie Xi and Andreas Heyden

APRIL 13, 2020

ACS CATALYSIS

READ ▶

### Insight into the Influence of the Graphite Layer and Cobalt Crystalline on a ZIF-67-Derived Catalyst for Fischer-Tropsch Synthesis

Yao Chen, Zhenhua Li, et al.

FEBRUARY 16, 2021

ACS APPLIED MATERIALS & INTERFACES

READ ▶

### Dynamic Phase Transition of Iron Oxycarbide Facilitated by Pt Nanoparticles for Promoting the Reverse Water Gas Shift Reaction

Hanning Chen, Zhaoxiong Xie, et al.

NOVEMBER 18, 2021

ACS CATALYSIS

READ ▶

Get More Suggestions >